UNIVERSIDAD NACIONAL AUTÓNOMA DE MEXICO
MAESTRÍA EN CIENCIAS (ASTROFÍSICA)
INSTITUTO DE FÍSICA
ASTROFÍSICA TEÓRICA

EFFECT OF THE METALLICITY OF THE IGM IN THE
LYMAN-α FOREST CORRELATION FUNCTION

TESIS
QUE PARA OPTAR POR EL GRADO DE:
MAESTRA EN CIENCIAS FÍSICAS (ASTROFISICA)

PRESENTA:
ANDREA MUÑOZ GUTIÉRREZ

TUTOR PRINCIPAL
DR. AXEL RICARDO DE LA MACORRA PETTERSSON MORIEL
INSTITUTO DE FÍSICA

MIEMBROS DEL COMITÉ TUTOR
DRA. MARIANA VARGAS MAGAÑA
INSTITUTO DE FÍSICA

DR. JOSÉ OCTAVIO VALENZUELA TIJERINO
INSTITUTO DE ASTRONOMÍA

CIUDAD UNIVERSITARIA, CD. MX. , JULIO DE 2019

Effect of the Metallicity of the IGM in the Lyman-α Forest Correlation Function

Andrea Muñoz Gutiérrez
Supervised by Dr. Axel de la Macorra Pettersson

July 2019

2

Contents

Chapter 1

Abstract

The improvement of galaxy surveys (together with Cosmic Microwave Background Radiation (CMB) observations) has allowed to constrain cosmological parameters, as well as the development of high precision Cosmology. There are many aspects of the Universe that allow these constraints. Among these the Supernovae type Ia (SNIa), and Baryon Acoustic Oscillations (BAO) observations. Among the latter, the observations of different tracers, and of particular interest is the study Stof clustering of dark matter using the intergalactic medium (IGM) as such. This is done by analyzing the correlation of (IGM) overdensities via the Ly-α forest.

When simulating the IGM clouds they are usually simplified assuming they are made of hydrogen, and hosting only the Ly-α transition. When the correlation functions are computed for these simulations (mock catalogues), they present a bias when compared to those of the data of surveys (eBOSS [1]). To understand this bias, several phenomena should be added in the mock spectra. Among these, Damped Ly-α Absorbers (DLA), Broad Absorption Lines (BAL), High Column Densities (HCD), and of particular interest, metals.

The goal of this work is to understand the role of the presence of metals in the IGM clouds in the mentioned bias. This is achieved by adding absorptions of four Si transitions (SiII(1260), SiIII(1207), SiII(1190), and SiII(1193)) in the mock spectra and analyze the correlations they present with Ly-α transition and with each other, and then confronting them with the correlations computed with the data.

What was found is that the presence of metals in the spectra introduces bumps and anchors in the shape of the three-dimensional flux correlation function ξ_{3D}, as well as well defined peaks in the one-dimensional flux correlation function ξ_{1D}. Each of these contributions is due to the correlations of the mentioned Si lines with Ly-α absorptions in the forest. They are all individually added to the mock data, studied, quantified and tuned to understand their effect in ξ_{3D} and ξ_{1D}.

This test allows a better understanding of the data obtained in the 14th Data Release of the Extended Baryon Oscillation Spectroscopic Survey (eBOSS DR14 [2]) and in the near future will do so for the Dark Energy Spectroscopic Instrument (DESI [3], [4]).

Chapter 2

Introduction

2.1 ΛCDM Model

The standard model in Cosmology is ΛCDM. It is based on General Relativity and states a universe described by the Friedmann-Lemaître-Robertson-Walker metric:

$$ds^2 = c^2 dt^2 - a(t)^2 \left(\frac{dr^2}{1 - kr^2} + r^2 d\theta^2 + r^2 sen^2\theta d\phi \right)$$ (2.1)

(where the first term expresses the time dimension, and the next three to the spatial components; r, θ, ϕ the coordinates, $k = -1, 0, 1$ the curvature of the Universe ($k = -1$ is an open universe, $k = 0$ a flat one, and $k = 1$ a closed one), and $a(t)$ the *scale factor*, that describes the "size" of the Universe compared to the present time, where $a = a_0 = 1$) and made of regular matter (described by the Standard Model of Elementary Particles), an unknown kind of non relativistic matter (Cold Dark Matter - CDM) that interacts only gravitationally, and with an accelerated expansion described by a cosmological constant Λ with an equation of state given by $w = P/\rho = -1$ (P being the pressure, and ρ density), so that, taking the equation:

$$\rho = \rho_i \left(\frac{a}{a_i} \right)^{-3(w+1)}$$ (2.2)

valid for any fluid that follows the continuity equation, $\rho_\Lambda = \Lambda$, then $p_\Lambda = -\rho_\Lambda = \Lambda$

Observations also show that the Universe has a geometry very close to a flat one. Its components are approximately given in the proportions shown in figure 2.1. Depending on the probes to obtain these results they can vary around these values.
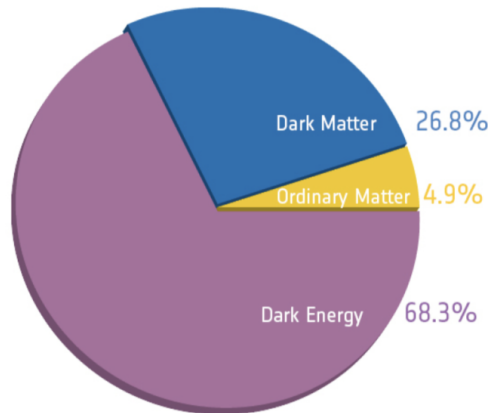
Figure 2.1: Pie chart showing the components of the universe and their (approximate) proportions according to the ΛCDM model. [5]

The stages of the Universe described by this model (shown schematically in figure 2.2) are the following:

- Inflation: this is the initial period of the Universe, when it grows in a nearly exponential rate and primordial perturbations in the relativistic plasma occurred.

- Recombination: fluctuations in the primordial plasma (protons and electrons with photons coupled via Thompson scattering) propagated through it as sound waves and produced over and underdensities. As the Universe expanded its temperature dropped, reaching the temperature where photons decoupled from protons and electrons, allowing neutral hydrogen to form. This caused the over and underdensity patterns to "freeze", and leave an imprint in this first emitted light (Cosmic Microwave Background Radiation, CMB) as well as in baryonic matter, which started clumping due to gravitational attraction and falling into dark matter potential wells, and eventually evolved into structure until forming the Baryon Acoustic Oscillations (BAO) (explained in 2.4) visible in the distribution of galaxies in the Large Scale Structure of the Universe.

- Dark Ages and Reionization: After recombination and until the Cosmic Dawn, the Universe is not observable in almost any wavelength (there are emissions in the 21 cm line). This stage is known as *Dark Ages*. During this time matter collapses gravitationally forming overdense regions (defined by BAO), which lead to dark matter haloes and formation of gas clouds (also collapsing gravitationally) and the first stars. The radiation coming from these stars and early Active Calactic Nuclei (AGN) ionized the Inter Galactic Medium (IGM).

- Accelerated expansion of the Universe: After several Gigayears (Gyr), the Universe turned its expansion into an accelerated one as a consequence of the negative pressure attributed to the domain of dark energy (or the cosmological constant Λ) over radiation and matter, opposing to gravitational attraction. [6]
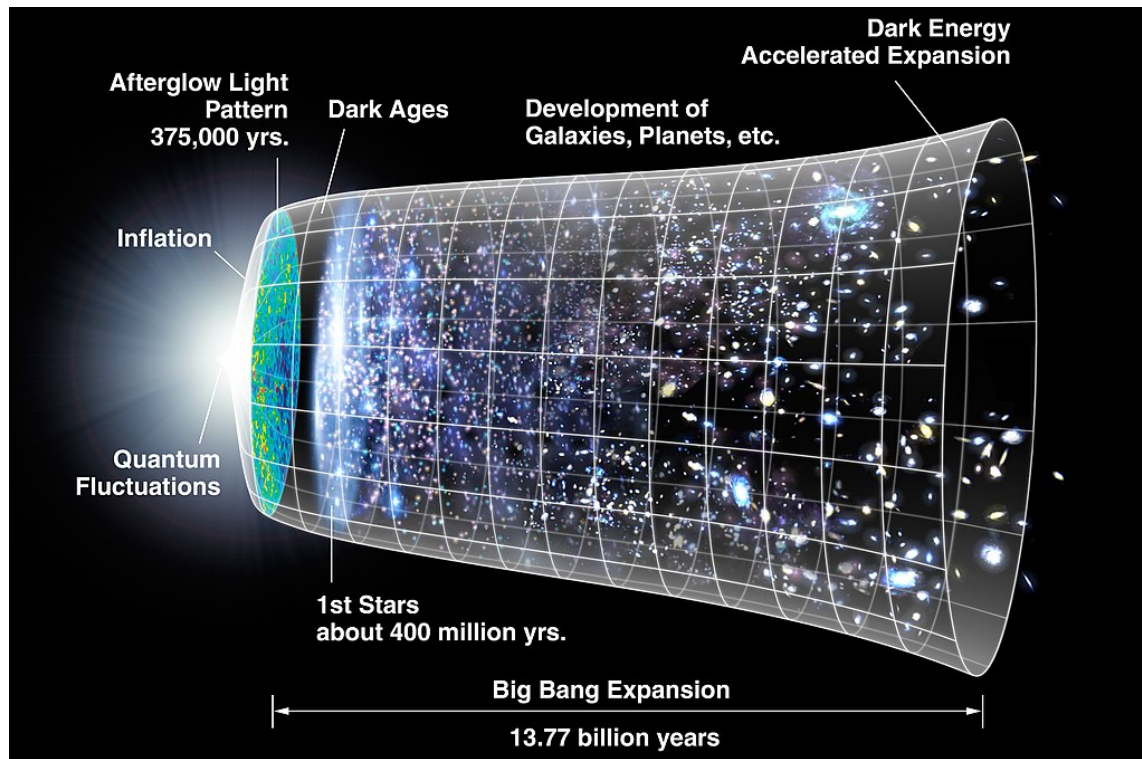
Figure 2.2: Different chronological stages of the evolution of the Universe through its 13.7 Gyr. [6]

This popularity of this model is due to its success explaining several phenomenae. Among these CDM explains the observed kinematics in galaxies and clusters, which is not the one expected to be observed if considering only the baryonic matter. It also is consistent with the amplitude of the peaks of the CMB power spectrum, which tell the abundance of baryonic matter with respect to the dark one, the observation of gravitational lensing, as well as the fact that there are about 80% disk galaxies while galaxy disks are dynamically unstable. The CMB power spectrum's first peak observations show the Universe has a geometry very close to a flat one, nonetheless there is an amount of matter that only explains about 30% of it. The other 70% is attributed to the cosmological constant Λ, which explains the accelerated expansion of the Universe. This expansion has been observed using SNIa and Gamma Ray Bursts (GRB) as standard candles to measure distances ans using BAO as standard rulers. This model also predicts the formation of light elements (deuterium, helium, lithium, and berillium) in the early universe as a consequence of reheating. If there had not been such, the existence of light elements would have to be explained by the stellar nuclear processes, which is not enough to explain the observed abundances. [7] There are several experiments (done on Earth, balloons, and satellites) that present results that are consistent with the ΛCDM model and with each other (although some of them present some tensions, for example in the measurement of H_0, as shown in figure 2.3 [8]). Among these, the CMB has been studied by COBE (Cosmic Background Explorer [9]), BOOMERanG (Balloon Observations Of Millimetric Extragalactic Radiation ANd Geophysics [10]), MAXIMA (Millimeter Anisotropy eXperiment Imaging Array [11]), ACBAR (Arcminute Cosmology Bolometer Array Receiver [12]), WMAP (Wilkinson Microwave Anisotropy

Probe [13]), and PLANCK [**?**] (parameters obtained with this mission are found in figure 2.4 [8]), BAO have been studied by BOSS (Baryon Oscillation Spectroscopic Survey [14]), eBOSS (Extended Baryon Oscillation Spectroscopic Survey [1]), WiggleZ [15], DES (Dark Energy Survey [16] [17]), 6dFGS (Six-degree-Field Galaxy Survey [18]), in the near future DESI (Dark Energy Spectroscopic Instrument [3] [4]), and SNIa are studied by the SCP (Supernova Cosmology Project [19]), and Pantheon sample [20].

Figure 2.3: Constraints on the Hubble parameter and Ω_m in the ΛCDM model. Contours represent 68% and 95% of the probability. [8]

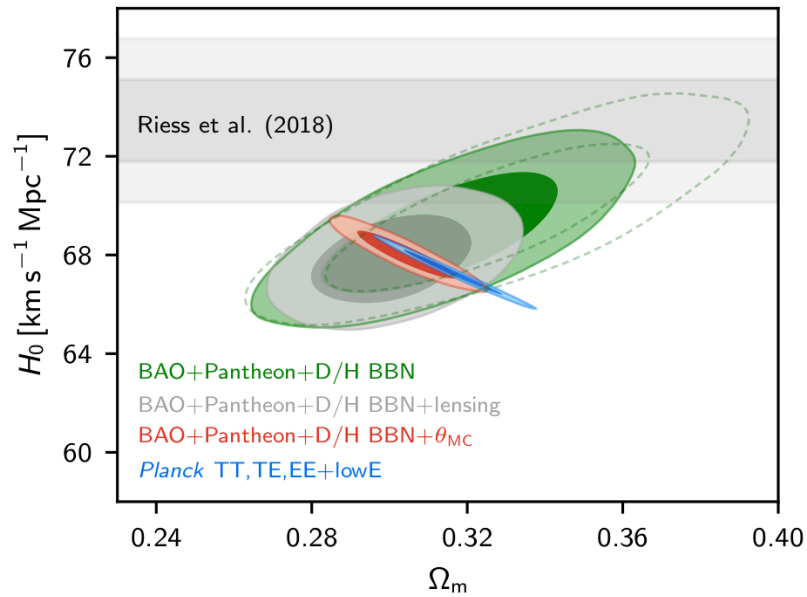| Parameter	TT,TE,EE+lowE 68% limits	TT,TE,EE+lowE+lensing+BAO 68% limits
$\Omega_b h^2$	0.02236 ± 0.00015	0.02242 ± 0.00014
$\Omega_c h^2$	0.1202 ± 0.0014	0.11933 ± 0.00091
$100\theta_{MC}$	1.04090 ± 0.00031	1.04101 ± 0.00029
τ	$0.0544^{+0.0070}_{-0.0081}$	0.0561 ± 0.0071
$\ln(10^{10}A_s)$	3.045 ± 0.016	3.047 ± 0.014
n_s	0.9649 ± 0.0044	0.9665 ± 0.0038
H_0 [km s^{-1} Mpc^{-1}]	67.27 ± 0.60	67.66 ± 0.42
Ω_Λ	0.6834 ± 0.0084	0.6889 ± 0.0056
Ω_m	0.3166 ± 0.0084	0.3111 ± 0.0056
$\Omega_m h^2$	0.1432 ± 0.0013	0.14240 ± 0.00087
$\Omega_m h^3$	0.09633 ± 0.00029	0.09635 ± 0.00030
σ_8	0.8120 ± 0.0073	0.8102 ± 0.0060
$S_8 \equiv \sigma_8(\Omega_m/0.3)^{0.5}$	0.834 ± 0.016	0.825 ± 0.011
$\sigma_8\Omega_m^{0.25}$	0.6090 ± 0.0081	0.6051 ± 0.0058
z_{re}	7.68 ± 0.79	7.82 ± 0.71
$10^9 A_s$	$2.101^{+0.031}_{-0.034}$	2.105 ± 0.030
$10^9 A_s e^{-2\tau}$	1.884 ± 0.012	1.881 ± 0.010
Age [Gyr]	13.800 ± 0.024	13.787 ± 0.020
z_*	1089.95 ± 0.27	1089.80 ± 0.21
r_* [Mpc]	144.39 ± 0.30	144.57 ± 0.22
$100\theta_*$	1.04109 ± 0.00030	1.04119 ± 0.00029
z_{drag}	1059.93 ± 0.30	1060.01 ± 0.29
r_{drag} [Mpc]	147.05 ± 0.30	147.21 ± 0.23
k_D [Mpc^{-1}]	0.14090 ± 0.00032	0.14078 ± 0.00028
z_{eq}	3407 ± 31	3387 ± 21
k_{eq} [Mpc^{-1}]	0.010398 ± 0.000094	0.010339 ± 0.000063
$100\theta_{s,eq}$	0.4490 ± 0.0030	0.4509 ± 0.0020

Figure 2.4: Parameters for the base-ΛCDM model from CMB power spectra, CMB lensing, and BAO at 68% intervals. [8]

2.2 Distances

The FLRW metric (equation 2.1) allows the calculation of cosmological distances. To make this, (following the discussion in [21] and [22]) we consider $d\Omega = r^2 d\theta^2 + r^2 sen^2\theta d\phi = 0$ in the expression. Doing so, we simplify the measurement by choosing convenient coordinate axes.

We define the following distances:

Comoving Distance

The *comoving distance* is a fixed distance between two points r_1 and r_2. This distance does not change with the expansion of the Universe and it is given by:

$$\Delta r = \int_{r_1}^{r_2} \frac{1}{\sqrt{1 - kr^2}} \, dr \tag{2.3}$$

$$\Delta r = \begin{cases} r_2 - r_1 & si \quad k = 0 \\ arcsen(r_2) - arcsen(r_1) & si \quad k = 1 \\ arcsenh(r_2) - arcsenh(r_2) & si \quad k = -1 \end{cases} \tag{2.4}$$

Physical Distance

The *physical dostance* is the real distance between two points with comoving coordinates r_1 and r_2, and does change with the expansion of the Universe. It is given by:

$$D = \int_{r_1}^{r_2} dl \tag{2.5}$$

with $dl = \frac{a(t)}{\sqrt{1-kr^2}} dr$ the spatial part of 2.1, hence:

$$D(t) = a(t) \int_{r_1}^{r_2} \frac{1}{\sqrt{1-kr^2}} dr \tag{2.6}$$

$$D(t) = a(t)\Delta r \tag{2.7}$$

For two given times t_a and t_b, the physical distances are:

$$D(t_a) = a(t_a) \int_{r_1}^{r_2} \frac{1}{\sqrt{1-kr^2}} dr \tag{2.8}$$

$$D(t_b) = a(t_b) \int_{r_1}^{r_2} \frac{1}{\sqrt{1-kr^2}} dr. \tag{2.9}$$

Using these two expressions, and considering tha comoving distance does not change with the expansion of the Universe, the physical distance at t_a, $D(t_a)$ can be computed if the scale factor a is known for these two times ($a(t_a)$ and $a(t_b)$) and the distance at t_b, $D(t_b)$:

$$D(t_a) = \frac{a(t_a)}{a(t_b)} D(t_b) \tag{2.10}$$

Proper Distance

The *proper distance* is the distance traveled by a light beam. It is given by:

$$d_p(t) = c \int_{ti}^{t} dt = c(t - t_i). \tag{2.11}$$

By definition, for a light beam $ds^2 = 0$, so if $d\phi$ and $d\theta$ are zero, we have:

$$dt = \frac{a(t)dr}{\sqrt{1-kr^2}}, \tag{2.12}$$

if $c = 1$:

$$d_p(t) = a(t) \int_{r_1}^{r_2} \frac{1}{\sqrt{1-kr^2}} dr = a(t) \int_{t_i}^{t} \frac{1}{a(t')} dt'. \tag{2.13}$$

If we take $t = t_i = 0$ as an initial time, and $t = t_0$ today's time as the final time, the proper distance turns into the distance to the horizon, which is the causally connected portion of the universe to an observer:

$$d_H(t_0) = a(t_0) \int_0^{t_0} \frac{1}{a(t)} \, dt \tag{2.14}$$

In the different epochs of the Universe different fluids (radiation, matter, Dark Energy) coexist. The distance to the horizon depends on this. Let us take the Friendmann equation:

$$H = \sqrt{\frac{8\pi G\rho}{3} - \frac{k}{a^2}} \tag{2.15}$$

with

$$\rho = \sum_i \rho_i = \rho_r + \rho_m + \rho_\Lambda = \rho_{r_o}\left(\frac{a}{a_0}\right)^{-4} + \rho_{m_o}\left(\frac{a}{a_0}\right)^{-3} + \rho_{\Lambda_0} \tag{2.16}$$

Multiplying and deviding this expression by the critical density measured today, $\rho_{c_0} = \frac{3H_0^2}{8\pi G}$, and defining $\Omega_i = \frac{\rho_i}{\rho_c}$ the density can be expressed by:

$$\rho = \rho_{c_0}\left(\left(\frac{\rho_{r_o}}{\rho_{c_o}}\right)\left(\frac{a}{a_0}\right)^{-4} + \left(\frac{\rho_{m_o}}{\rho_{c_o}}\right)\left(\frac{a}{a_0}\right)^{-3} + \left(\frac{\rho_{\Lambda_o}}{\rho_{c_o}}\right)\right) \tag{2.17}$$

$$= \rho_{c_0}\left(\Omega_{r_0}\left(\frac{a}{a_0}\right)^{-4} + \Omega_{m_0}\left(\frac{a}{a_0}\right)^{-3} + \Omega_{\Lambda_0}\right), \tag{2.18}$$

And H can be expressed as:

$$H = H_0\sqrt{\frac{8\pi G\rho}{3H_0^2} - \frac{k}{a^2 H_0^2}} \tag{2.19}$$

$$= H_0\sqrt{\frac{8\pi G}{3H_0^2}\left(\rho_{c_0}\left(\Omega_{r_0}\left(\frac{a}{a_0}\right)^{-4} + \Omega_{m_0}\left(\frac{a}{a_0}\right)^{-3} + \Omega_{\Lambda_0}\right)\right) - \frac{k}{a^2 H_0^2}}, \tag{2.20}$$

identifying $\frac{k}{H_0^2 a_0^2} = \frac{8\pi G}{3H_0^2}\rho_0 - \frac{H_0^2}{H_0^2} = \Omega_{T_0} - 1$ (with Ω_{T_0} the total density, corresponding $\Omega_t = 1$ to a flat universe)

$$H = H_0\sqrt{\Omega_{r_0}\left(\frac{a}{a_0}\right)^{-4} + \Omega_{m_0}\left(\frac{a}{a_0}\right)^{-3} + \Omega_{\Lambda_0}\left(\frac{a}{a_0}\right)^{-2} - (1 - \Omega_{T_0})} \tag{2.21}$$

so, taking the expression $\int \frac{dt}{a(t)} = \int \frac{da}{a^2 H}$ for distance and substituting H:

$$\int \frac{dt}{a(t)} = \int \frac{da}{a^2 H} = \tag{2.22}$$

$$\frac{1}{H_0}\int \frac{da}{a^2} \frac{1}{\sqrt{\Omega_{r_0}\left(\frac{a}{a_0}\right)^{-4} + \Omega_{m_0}\left(\frac{a}{a_0}\right)^{-3} + \Omega_{\Lambda_0}\left(\frac{a}{a_0}\right)^{-2} - (1 - \Omega_{T_0})}}, \tag{2.23}$$

if the scale factor today is $a_0 = 1$ and $\omega_{k_0} = 1 - \Omega_{T_0}$, the expression reduces to:

$$\int \frac{dt}{a(t)} = \frac{1}{H_0}\int \frac{da}{a^2} \frac{1}{\sqrt{\Omega_{r_0} + \Omega_{m_0}a + \Omega_{\Lambda_0}^4 + \Omega_{k_0}a^2}}. \tag{2.24}$$

Luminosity Distance

There are objects in the universe whose intrinsic luminosity L can be known from its flux F, such as variable stars, SNIa, etc. When relating the flux to the luminosity of these objects, one can obtain an approximate distance to them. This defines the *luminosity distance* d_L. F and L are related by:

$$F = \frac{L}{4\pi d_L^2},\tag{2.25}$$

where L is:

$$L = \frac{E}{\delta t},\tag{2.26}$$

with E the energy of the photons involved, and δt a given timelapse. This flux changes due to the expansion on the Universe. So, for light:

$$\frac{\delta t_0}{\delta t_1} = \frac{\lambda_0}{\lambda_i} = \frac{a_0}{a(t_1)} = \frac{E_1}{E_0},\tag{2.27}$$

Where the quantities with the subindex 0 are measured nowadays, and subindex 1 the time when they were emitted. If on Earth, tday, we observe a luminosity of:

$$L_0 = \frac{E_0}{\delta t_0}.\tag{2.28}$$

from (2.27),

$$E_1 = \frac{a_0}{a(t_1)} E_0 \tag{2.29}$$

$$\delta t_1 = \frac{a(t_1)}{a_0} \delta t_0,\tag{2.30}$$

then

$$L_0 = \frac{E_0}{\delta t_0} = \left(\frac{a(t_1)}{a_o}\right)^2 \frac{E_1}{\delta t_1} = \left(\frac{a(t_1)}{a_o}\right)^2 L_1.\tag{2.31}$$

As said previously, the physical distance is related with the comoving distance by the scalefactor; for a given time t_1 and today t_0:

$$d(t_1) = a(t_1)\Delta r \tag{2.32}$$
$$d_0 = a_0 \Delta r.\tag{2.33}$$

So for t_1:

$$d(t_1) = \frac{a(t_1)}{a_0} d(t_0) = a(t_1)\Delta r.\tag{2.34}$$

S the flux observed today is:

$$F_0 = \frac{L_0}{4\pi d_o^2} = \left(\frac{a(t_1)}{a_o}\right)^2 \frac{L_1}{4\pi a_0^2(\Delta r)^2} = \frac{L_1}{4\pi a_0^2(\Delta r)^2(1+z)^2},\tag{2.35}$$

And the luminosity distance for an expanding universe is defined as:

$$d_L = a_0 \Delta r (1+z). \tag{2.36}$$

From the Friedmann equation:

$$H^2 = H_0^2 \left(\frac{8\pi G \rho}{3H_0^2} - \frac{k}{a^2 H_0^2} \right) = H_0^2 \left(\sum_i \Omega_{0_i} \left(\frac{a}{a_0} \right)^{-3(1+w)} - \frac{k}{a^2 H_0} \right), \tag{2.37}$$

where the sum is over all the components of the Universe (matter, radiation, dark energy, etc.). Substituting $k/a^2 H_0$ in terms of Ω_T:

$$H^2 = H_0^2 \left(\sum_i \Omega_{0_i} \left(\frac{a}{a_0} \right)^{-3(1+w)} + (1+\Omega_T) \left(\frac{a}{a_0} \right)^{-2} \right) \tag{2.38}$$

For light, $\Delta r = \int_{t_1}^{t_0} \frac{dt}{a(t)}$. With this, the comoving distance turns into:

$$\Delta r = \int \frac{da}{a^2 H_0 \left(\sum_i \Omega_{0_i} \left(\frac{a}{a_0} \right)^{-3(1+w)} + (1+\Omega_T) \left(\frac{a}{a_0} \right)^{-2} \right)^{(1/2)}} \tag{2.39}$$

And the luminosoty distance into:

$$d_L = \frac{a_0(1+z)}{a_0} \int_{a_0}^{a} \frac{da}{a^2 \left(\sum_i \Omega_{0_i} \left(\frac{a}{a_0} \right)^{-3(1+w)} + (1+\Omega_T) \left(\frac{a}{a_0} \right)^{-2} \right)^{(1/2)}}. \tag{2.40}$$

The luminosity distance can also be expressed in terms of z as:

$$d_L(z) = \frac{1}{H_0} \left(z + \frac{1}{2}(1-q_0)z^2 + ... \right) \tag{2.41}$$

Angular Distance

Lets consider an object of size D, at a distance d, that subtends an angular size θ. The angular-diameter size d_A is given by:

$$\theta = \frac{D}{d_A} \rightarrow d_A = \frac{D}{\theta} \tag{2.42}$$

To express d_A in terms of the FLRW metric, D represents the proper distance between two light signals emitted from two points with the same radial coordinate r_e at a time t_e, reaching the observer at t_0. D will then be the integral of the spatial part of the metric (2.1):

$$D = a_e r_e \int d\theta = \frac{a_0 r_e}{1+z} \theta \tag{2.43}$$

with $a_0 = a(t_0)$ and $a_e = a(t_e)$. Substituting this result in 2.42,

$$d_A = \frac{a_0 r_e}{1+z} = a_e r_e \tag{2.44}$$

In a space with no expansion, $d_A = d_L = d$, but in the cosmological context these values differ.

2.2.1   Cosmological Redshift

Due to the change of energy levels of electrons, photons are emitted (or absorbed) in the different elements of the periodic table at specific (and unique) wavelengths. These emissions/absorptions have an energy E given by the equation $E = h\nu = h/\lambda$ (being h the Planck constant, ν the frequency of the emission/absorption and λ its corresponding wavelength with $c = 1$). When the source that emits (or absorbs) moves away or closer to the observer, the wavelength of the emission (or absorption) appears shifted to the blue side of the electromagnetic spectrum (blueshifted, if getting closer) or the red side (redshifted, if moving away). Observations of galaxies show that when analyzing their spectra, they are redshifted. This is due to the expansion of the Universe.

To define the redshift z, lets consider a light beam emited by a galaxy at a time t_i from a position r_i. This beam is detected by the observer at a position $r = r_0 = 0$ and time t_0. From GR, by definition $ds^2 = 0$, so from the FRW metric:

$$dt = \frac{a(t)dr}{\sqrt{1 - kr^2}} \tag{2.45}$$

and

$$\int_{t_i}^{t_0} \frac{1}{a(t)}\, dt = \int_{r_i}^{r_0} \frac{1}{\sqrt{1 - kr^2}} \cdot dr \tag{2.46}$$

Let us also suppose that the wave starts to be emitted at a time t_i (will be observed at t_0), and at a time $ti + \delta t_i$ a different "part" of the same wave (will be observed at $t_0 + \delta t_0$). Since r_0 and r_i are comoving, from (2.46):

$$\int_{t_i + \delta t_i}^{t_0 + \delta t_0} \frac{1}{a(t)}\, dt = \int_{r_i}^{r_0} \frac{1}{\sqrt{1 - kr^2}}\, dx, \tag{2.47}$$

hence

$$\int_{t_i}^{t_0} \frac{1}{a(t)}\, dt = \int_{t_i + \delta t_i}^{t_0 + \delta t_0} \cdot \frac{1}{a(t)}\, dt \tag{2.48}$$

If we sum $\int_{t_0}^{t_i + \delta t_i} \frac{1}{a(t)}\, dt$ to both sides, we obtain:

$$\int_{t_i}^{t_i + \delta t_i} \frac{1}{a(t)}\, dt = \int_{t_0}^{t_0 + \delta t_0} \frac{1}{a(t)}\, dt. \tag{2.49}$$

We note that δt can be as small as needed, then the change in $a(t)$ is negligible in the $t, t + \delta t$ interval, so it is considered constant. Hence:

$$\frac{\delta t_i}{a(t_i)} = \frac{\delta t_0}{a(t_0)}. \tag{2.50}$$

The wavelengths corresponding to each wave are:

$$\lambda_i = c\delta t_i \tag{2.51}$$
$$\lambda_0 = c\delta t_0, \tag{2.52}$$

and we obtain:

$$\frac{\delta t_0}{\delta t_i} = \frac{a(t_0)}{a(t_i)} = \frac{\lambda_0}{\lambda_i} \tag{2.53}$$

From this expression we can see that if $a(t_0) > a(t_i)$, $\lambda_0 > \lambda_i$, which means that the observed wavelength is larger then it was when it was emited (i.e. redshifted). This shift is a consequence of the expansion of the Universe, and the objects that present this behavior are tracers of this expansion. This *cosmological redshift* (or *redshift*) z is defined as:

$$\frac{a(t_0)}{a(t_i)} = 1 + z = \frac{\lambda_0}{\lambda_i} \tag{2.54}$$

$$z = \frac{\lambda_0}{\lambda_1} - 1 = \frac{\lambda_0 - \lambda_1}{\lambda_1} \tag{2.55}$$

2.3   Large Scale Structure (LSS)

The patterns in galaxies and matter in scales larger than groups of galaxies is called the *Large Scale Structure* (LSS) of the Universe. These patterns are caused mainly by gravity, and contain filaments of galaxies, walls and voids, and are extended over several hundred million light years. Due to the resemblance with a spider web they are also known as the *Cosmic Web*. The LSS contains baryonic (visible) matter, which is a tracer of the non visible dark matter, and is studied observationally and theoretically in order to understand the different evolutionary stages of the Universe. Figure 2.5 shows a zoom of the Millenium-II simulation (Boylan-Kolchin et al. 2009), an N-body simulation of dark matter evolution in the ΛCDM model. [23] [24] [25]
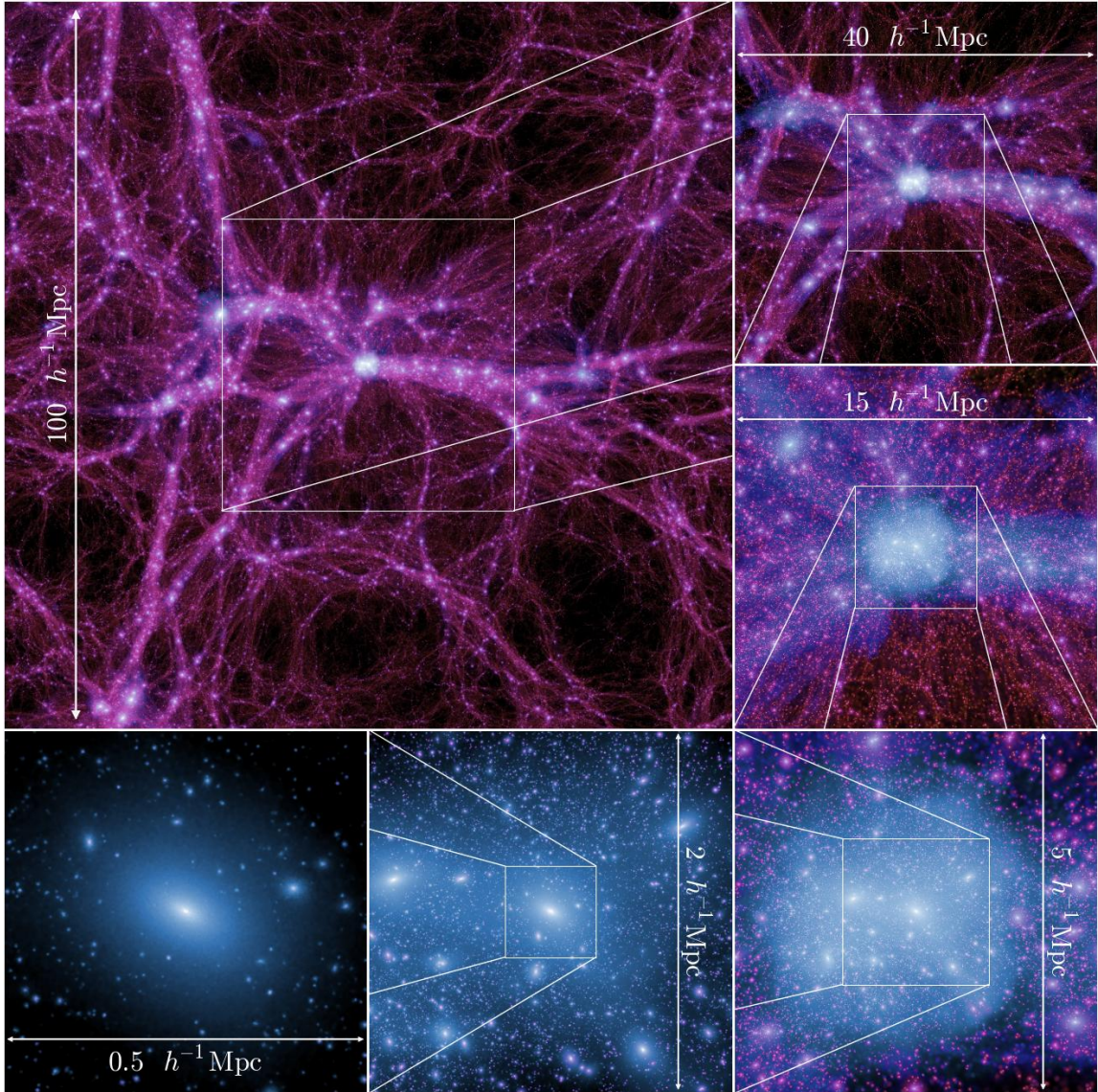
Figure 2.5: Simulated LSS in the Millennium-II Simulation, an N-body simulationof dark matter evolution using the parameters given by the ΛCDM model. [23]

2.3.1   Perturbation Theory and Structure Formation

To understand the formation and evolution of the large scale structure of the Universe inhomogeneities should be considered. IGM clouds, galaxies and clusters of galaxies have grown from small density perturbations caused by gravity.

For this analysis (based on [22] and [21]), initial density perturbations and their evolution in

an expanding Universe are considered. At first, a Newtonian perturbation theory in the linear regime description is done, (being the mean free path of the particles much smaller than the scales considered, baryonic gas and pressureless dust (colissionless dark matter) are in this regime - then IGM overdensities represented by the Ly-α forest are here included). The higher order perturbation theory is analyzed afterwards, since galaxy clustering is described by this approach.

Let ρ be the density and u the velocity of a non-relativistic fluid in a gravitational potential ϕ. Let $\vec{r}$ be the proper coordinate. The evolution of a fluid is given by the equation of continuity (mass conservation) 2.56, Euler equation (equation of motion) 2.57 and Poisson equation (which describes the gravitational field) 2.58:

$$\frac{D\rho}{Dt} + \rho \nabla_{\vec{r}} \cdot \vec{u} = 0, \tag{2.56}$$

$$\frac{D\vec{u}}{Dt} = -\frac{\nabla \vec{r} P}{\rho} - \nabla \vec{u} \phi \tag{2.57}$$

$$\nabla_{\vec{r}}^2 \phi = 4\pi G \rho. \tag{2.58}$$

Let us define the convective time derivative as the time derivative of a quantity that moves with the fluid:

$$\frac{D}{Dt} \equiv \frac{\partial}{\partial t} + \vec{u} \cdot \nabla_{\vec{r}} \tag{2.59}$$

To introduce the time evolution of the perturbations in an expanding universe describes by the FLRW metric, the propper coordinate $\vec{r}$ is written in terms of the comoving ones $\vec{x}$ as:

$$\vec{r} = a(t)\vec{x} \tag{2.60}$$

and the proper velocity $\vec{u} = \dot{\vec{r}}$ at a point $\vec{x}$ as:

$$\vec{u} = \dot{a}(t)\vec{x} + \vec{v} \tag{2.61}$$

with $\vec{v} \equiv a\dot{\vec{x}}$ the peculiar velocity describing the mtion of the fluid relative to a comoving observer with the background (fundamental observer) at $\vec{x}$. The time and spatial derivatives transform as following:

$$\nabla_{\vec{r}} \to \frac{1}{a} \nabla_{\vec{v}} \tag{2.62}$$

$$\frac{\partial}{\partial t} \to \frac{\partial}{\partial t} - \frac{\dot{a}}{a} \vec{x} \cdot \nabla_{\vec{x}}. \tag{2.63}$$

Now, the perturbed density ρ is written as:

$$\rho(\vec{x}, t) = \bar{\rho}(t)[1 + \delta(\vec{x}, t)], \tag{2.64}$$

So equations 2.56, 2.57, and 2.58 rewritten in comoving coordinates are:

$$\frac{\partial \delta}{\partial t} + \frac{1}{a} \nabla_{\vec{x}} \cdot [(1 + \delta)\vec{v}] = 0 \tag{2.65}$$

$$\frac{\partial \vec{v}}{\partial t} + \frac{\dot{a}}{a}\vec{v} + \frac{1}{a}(\vec{v} \cdot \nabla_{\vec{x}})\vec{v} = -\frac{\nabla_{\vec{x}}\Phi}{a} - \frac{\nabla_{\vec{x}}P}{a\bar{\rho}(1+\delta)} \tag{2.66}$$

$$\nabla_{\vec{x}}^2 \Phi = 4\pi G\bar{\rho}a^2\delta, \text{ with } \Phi = \phi + \frac{a\dot{a}x^2}{2} \tag{2.67}$$

Considering that $\frac{\nabla P}{\bar{\rho}} = c_s^2 \nabla\delta$, where c_s i sthe adiabatic sound speed, given by $c_s = \left(\frac{\partial P}{\partial \rho}\right)^{1/2}$, equation 2.66 can be rewritten as:

$$\frac{\partial \vec{v}}{\partial t} + \frac{\dot{a}}{a}\vec{v} + \frac{1}{a}(\vec{v} \cdot \nabla_{\vec{x}})\vec{v} = -\frac{\nabla_{\vec{x}}\Phi}{a} - \frac{c_s^2}{a}\frac{\nabla_{\vec{x}}\delta}{(1+\delta)} \tag{2.68}$$

As mentioned before, the approach for the IGM is the one of linear perturbations. δ and $\vec{v}$ are small enough so that the nonlinear terms in equations 2.65 and 2.66 can be neglected. Equation 2.65 is rewritten as:

$$\frac{\partial \delta}{\delta t} + \frac{1}{a}\nabla_{\vec{r}} \cdot \vec{v} = 0 \tag{2.69}$$

and equation 2.66 as:

$$\frac{\partial \vec{v}}{\partial t} + \frac{\dot{a}}{a}\vec{v} = -\frac{\nabla_{\vec{x}}\Phi}{a} - \frac{c_s^2}{a}\nabla_{\vec{x}}\delta \tag{2.70}$$

where, if the curl is computed to both sides, we obtain $\nabla \times \vec{v} \propto a^{-1}$. If the derivative of 2.69 is computed with respect to t, and using 2.67 and 2.70 we get:

$$\frac{\partial^2 \delta}{\partial t^2} + 2\frac{\dot{a}}{a}\frac{\partial \delta}{\partial t} = 4\pi G\bar{\rho}\delta + \frac{c_s^2}{a^2}\nabla^2\delta \tag{2.71}$$

The term $2\frac{\dot{a}}{a}\frac{\partial \delta}{\partial t} = 2H\frac{\partial \delta}{\partial t}$ is the Hubble drag term, it tends to the damping of perturbations as the Universe grows. The term $4\pi G\bar{\rho}\delta$ is the gravitational one. This causes the growth of perturbations. The term $\frac{c_s^2}{a^2}\nabla^2\delta$ reperesents the spatial variations in density.

The perturbations $\delta(\vec{x}, t)$ can be transformed into $\delta_{\vec{k}}(t)$ (x being a comoving coordinates, and k wavevectors in comoving units) using its Fourier transform, so that:

$$\delta_{\vec{k}}(t) = \frac{1}{V} \int \delta(\vec{x}, t)e^{-i\vec{k}\cdot\vec{x}}d^3\vec{x} \tag{2.72}$$

being V the volume where the perturbation is assumed to be periodic. Hence the evolution equation for the modes $\delta_{\vec{k}(t)}$ is given by the Fourier transform of equation 2.73. Using that $\nabla \to i\vec{k}$ and $\nabla^2 \to -\vec{k}^2$ in the Fourier transformation, this is:

$$\frac{d^2\delta_{\vec{k}}}{dt^2} + 2H\frac{d\delta_{\vec{k}}}{dt} = \left[4\pi G\bar{\rho} - \frac{k^2c_s^2}{a^2}\right]\delta \tag{2.73}$$

In a Universe without expansion ($H = 0$) the solutions to this equation are:

$$\delta_{veck(t)} = \delta_k i e^{i(\omega t - i\vec{k}\cdot\vec{r})}\bar{\rho} \tag{2.74}$$

where ω is given by:

$$\omega^2 = c_s^2 k^2 - 4\pi G\bar{\rho} \tag{2.75}$$

and $k = 2\pi/\lambda$ the wavenumber of the oscillation.

w^2 can meet one of these conditions:

$w^2 > 0 \Rightarrow$ the pressure term dominates over the gravity one, and the perturbations oscillate as soundwaves.

$w^2 < 0 \Rightarrow$ the gravitational term dominates over the pressure one, and the perturbations grow (or decrease) exponentially.

There is a value for k for which w will be imaginary. This is k_J (Jeans' wavenumber), given by:

$$k_J \equiv \frac{\sqrt{4\pi G\bar{\rho}}}{c_s} \tag{2.76}$$

For this value the frequency of the oscillations is zero. For $k > k_J$ (small scales), the pressure term dominates over the gravitational one, and the perturbations oscillate as soundwaves. On the contrary, $k < k_J$ (big scales) the gravitational term dominates, the frequency w is be imaginary, and the perturbations grow exponentially.

Now, in a Universe with expansion ($H \neq 0$) with a non-relativistic fluid (matter), we analyze the evolution of δ as a function of the scale factor a. We take again equation 2.73. We consider the fact that $a = kt^{2/3}$, and $H = \frac{\dot{a}}{a} = \frac{2}{3t}$, and we take:

$$4\pi G\bar{\rho} = \frac{3}{2}H^2 = \frac{2}{3}\frac{1}{t^2}. \tag{2.77}$$

Let us propose an ansatz for δ, and take its derivatives:

$$\delta = \delta_i t^\alpha \tag{2.78}$$
$$\dot{\delta} = \frac{\alpha}{t}\delta \tag{2.79}$$
$$\ddot{\delta} = \frac{\alpha(\alpha-1)}{t^2}\delta \tag{2.80}$$

Substituting 2.78, 2.79, and 2.80 in 2.73, and factorizing $\frac{\delta}{t^2}$:

$$\frac{\delta}{t^2}\left[\alpha(\alpha-1) + \frac{4}{3}\alpha - \frac{2}{3}\right] = 0, \tag{2.81}$$

then

$$\alpha^2 + \frac{1}{3}\alpha - \frac{2}{3} = 0. \tag{2.82}$$

The solutions for this equation are $\alpha = -1$ and $\alpha = 2/3$. So for matter domation epoch, we have that the growing perturbation $\delta \sim t^{2/3} \sim a$, which means it grows as the scale fator.

2.4   Baryon Acoustic Oscillations (BAO)

Before the recombination epoch protons, electrons and photons were coupled fluids making a plasma where radiation pressure of the photons tended to go away and gravity tended to collapse in dark energy potential wells. This "battle" between radiation and matter caused the plasma to oscillate.

When the temperature of the Universe decreased due to its expansion and the photons ceased to interact with electrons, electrons and protons formed neutral hydrogen and the Universe became transparent for photons, which travelled freely accross the Universe to form the CMB, and the last oscillation *froze* imprinting a pattern of baryons. Gravitational interaction led to the formation of structure which evolved into the LSS pattern explained before.

Figure 2.6 from Eisenstein et al. (2007) shows the different stages (in redshift z) of the process in which BAO were formed. At first e^- and p^+ were coupled in the dark matter gravitational potential wells. The second pannel shows how the coupled plasma is dragged by the radiation pressure of photons. Eventually, when the temperature coonditions allowed it (as explained before), photons decoupled from this plasma (shown in the fourth panel, $z \approx 1081$), leaving an imprint of baryons and hereafter traveling freely through the Universe. Some of the baryons fell back in the potential well and some others stayed frozen in the last oscillation. The radius of this frozen pattern is known as the BAO scale. The last panel shows how at $z = 10$, when the dark ages finished and the first light sources (stars) were formed (reionization epoch) the BAO structure was already formed.
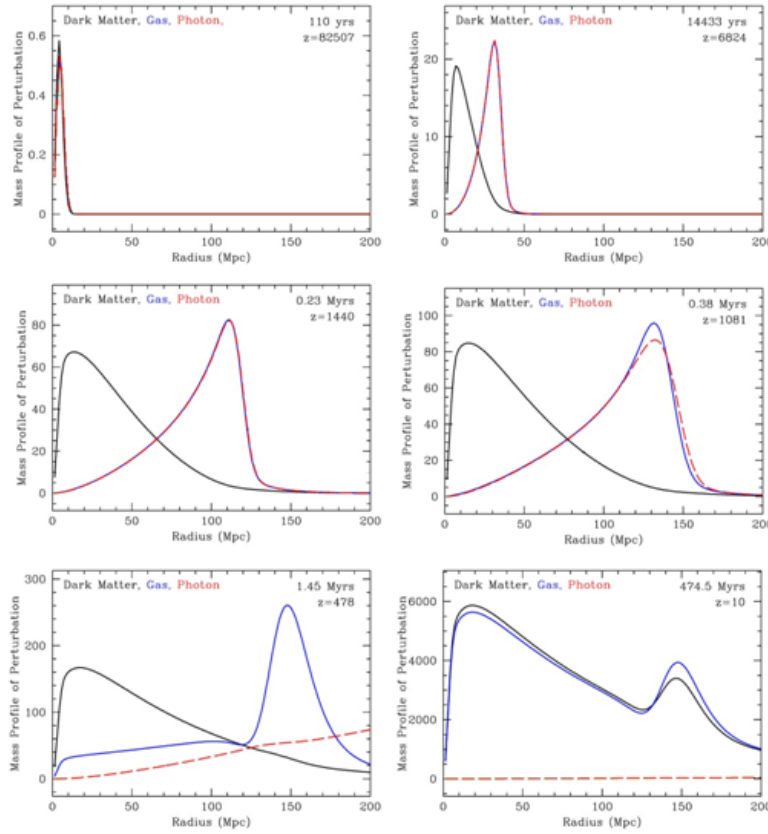
Figure 2.6: Snapshots of the process in which the BAO were formed in different epochs (redshifts z). The black lines represent dark matter, the blue ones represent baryons, and the red represent photons.

The *Baryon Acoustic Oscillations* are these evolved matter density oscillations that generate patterns in the distribution of objects (galaxies, quasars, IGM clouds, etc.) in the Universe. The imprint in this distribution in the LSS (shown schematically in figure (2.7)) caused by the propagation of soundwaves in the pre-recombination epoch is seen as a pronounced peak (the BAO peak) in the two-point correlation function and the anisotropy spectrum of the Cosmic Microwave Background (CMB).
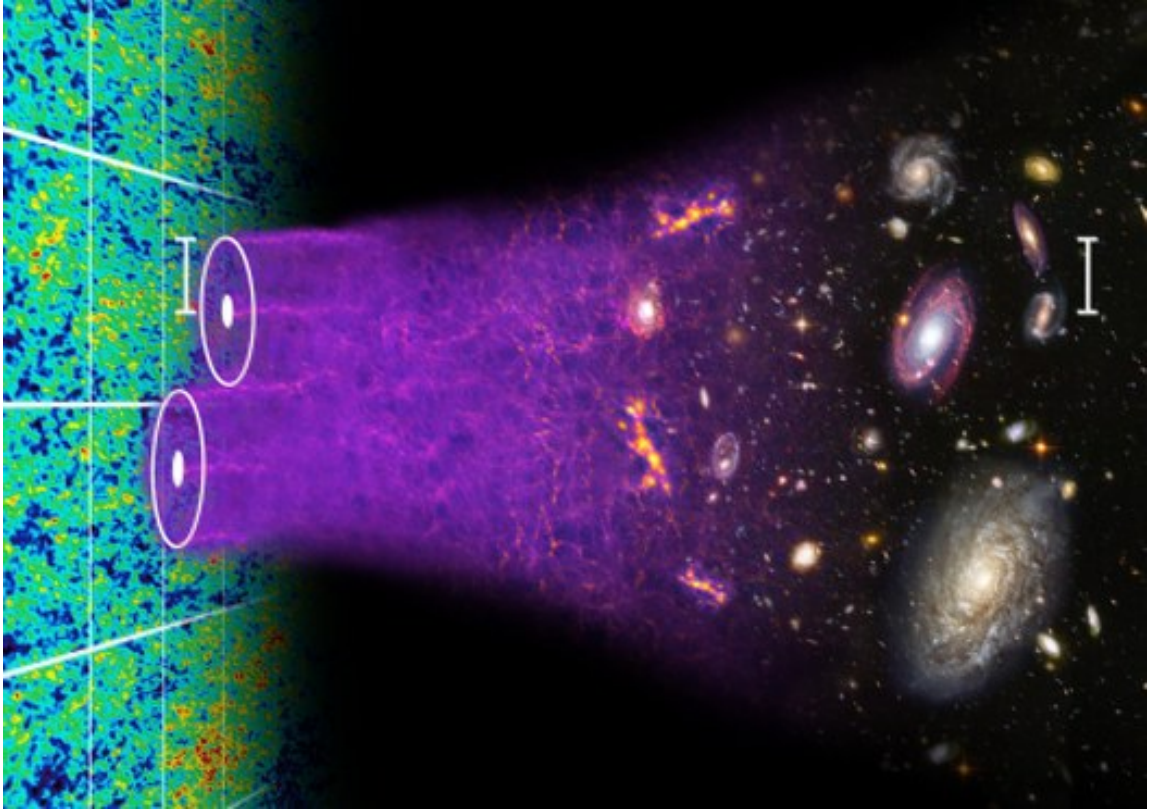
Figure 2.7: Schematical evolution of CMB anisotropies into the distribution of matter imprinted in the Large Scale Structure as Baryon Acoustic Oscillations. [26]

The position of the BAO peak centered on a comoving distance r_d at the drag epoch determines the ratio $D_M(z)/r_d$, where $D_M(z) = (1+z)D_A(z)$ is the comoving angular distance and $D_H(z)/r_d$ (where the Hubble distance is $D_H(z) = c/H(z)$ at a given (observed) redshift), relative to the sound horizon. These quantities depend on other cosmological parameters, hence these are constrained by the observation of the BAO peak. This peak is used as a *standard ruler*, since this scale is frozen, it allows to measure distances in the LSS, a scheme of this technique is shown in figure 2.8. [27] [?] [28]
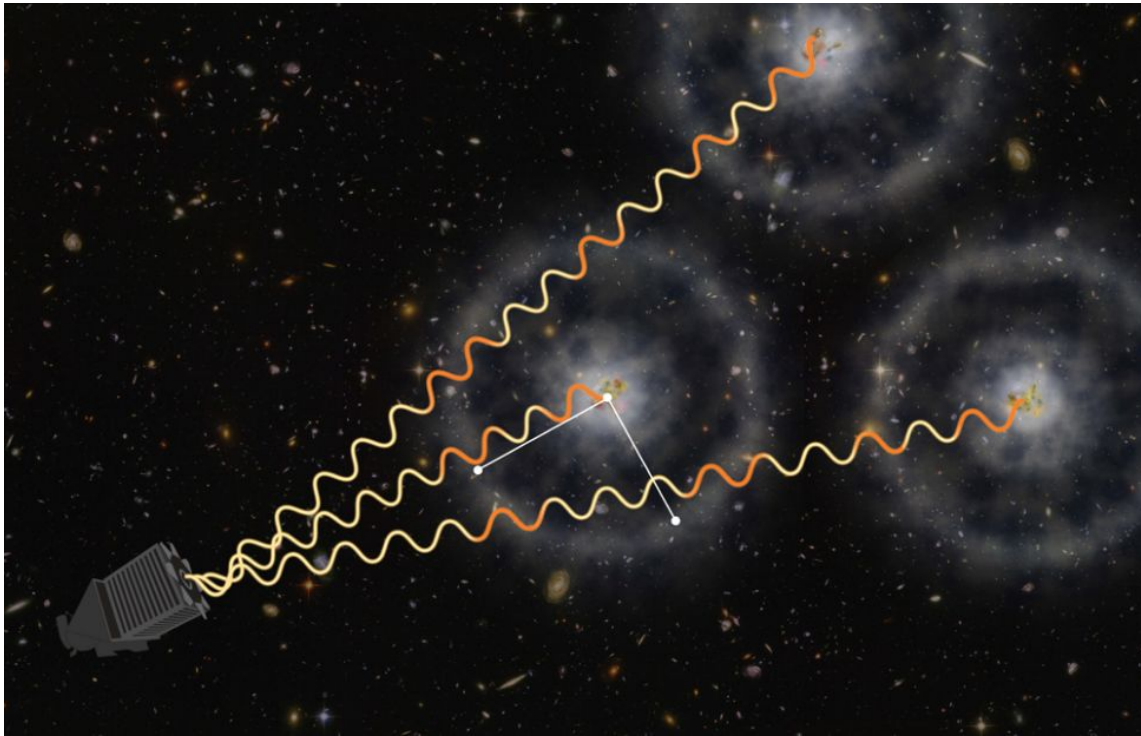
Figure 2.8: Scheme of the measurement of the BAO scale. Since this is a frozen scale, it can be used as standard ruler. Illustration by Zosia Rostomian, Lawrence Berkeley National Laboratory, and Andreu Font-Ribera, BOSS Lyman-alpha team, Berkeley Lab.

2.5 LSS Surveys

In the 1920s and 30s Edwin Hubble discovered cepheid stars in farway *spiral nebulae* and realized by estimating their distance to us that they were actually bodies outside the Milky Way. He then started studying and classifying them according to their morphologies (making the Hubble sequence, also known as the Hubble tuning fork diagram shown in figure 2.9), and also discovered, by observing a redshift in their spectra, that these galaxies were drifting away from one another following what is called the Hubble-Lemaître Law, with a velocity given by $v = Hr$, where v is the recessional velocity of the galaxies, r is its distance from the observer, and H the Hubble constant. Since this relation is seen in every direction, it was concluded from these observations that the Universe is expanding.

Figure 2.9: Scheme of the Hubble sequence of galaxy morphologies. [22]

As astronomical observations improved, and technology and the theoretical understanding of the Universe evolved, the three-dimensional mapping of objects in the Universe (using their position in the sky and redshift) became more precise and with it the calculation of H, given by:
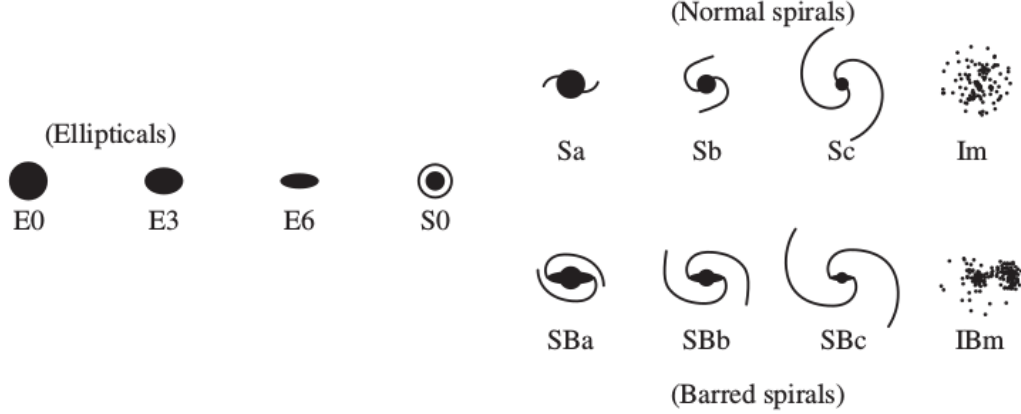
$$H(a) = H_0 \sqrt{\Omega_{r_0} \left(\frac{a}{a_0}\right)^{-4} + \Omega_{m_0} \left(\frac{a}{a_0}\right)^{-3} + \Omega_{\Lambda_0} \left(\frac{a}{a_0}\right)^{-2} - (1 - \Omega_{T_0})} \qquad (2.83)$$

using different techniques. With time, more and more LSS surveys have been designed and with them lots of data analyzed. This *evolution* of the observations has lead to an era of high precision Cosmology, where thousands of objects at high redshifts have increased the size and depth of the existent maps of the Universe. Among the tens of surveys currently or recently obtaining/reducing data or currently being designed are the Dark Energy Survey, Sloan Digital Sky Survey, and Dark Energy Spectroscopic Instrument. The two lattest are of particular interest for the development of this research.

2.5.1   SDSS - BOSS/eBOSS

The *Sloan Digital Sky Survey* (SDSS) is a redshift survey that consists of two twin 2.5m telescopes: the The Sloan Foundation Telescope at Apache Point Observatory (APO, south east New Mexico) and The Irénée du Pont Telescope at Las Campanas Observatory (northern Chile, used for southern hemisphere observations for SDSS-IV), and the NMSU 1-meter telescope at APO for bright sources. SDSS takes spectrographic and photometric images of surces (mainly galaxies and quasars) and has given data since its Early Data Release (EDR) in 2001. [29] The telescopes have two instruments: a CCD camera that takes images almost simultaneously in the bands u, g, r, i, and z in nights with good observation conditions and no moon, and two spectrographs that use fiber optics to take the spectra of 640 objects selected from the imaging data, and take the data during the other nights.

For cosmological purposes two redshift surveys have been made within SDSS-III and SDSS-IV respectively. The Baryon Oscillation Spectroscopic Survey (BOSS), which mapped the distribution of luminous red galaxies (LRG) and quasars (QSO) to detect the BAO characteristic scale ($\approx$

$150Mpc$) imprinted in it, and the Extended Baryon Oscillation Spectroscopic Survey (eBOSS), which is an extension of BOSS and has the goal of improving constraints on the nature of dark energy by observing galaxies (Luminous Red Galaxies - LRG, and Emission Line Galaxies - ELG) and quasars from $0.6 < z < 3$ (when cosmic expansion transitioned from deceleration to acceleration), signifficantly improving the data obtained by BOSS (provide BAO distance with a precision of 1% at $z = 0.7$ (for LRGs), 2% at $z = 0.85$ (for ELGs), and 2% at $z = 1.5$ (for quasars), and improved measurement of the BAO measurement by the Lyman-α forest in 120,000 new spectra, as well as measurements of the Redshift Space Distortions (RSD) and the non-Gaussianity of the primordial density field) which makes eBOSS the largest volume survey of the Universe to date. Figure (2.10) shows how deep in redshift are BOSS and eBOSS surveys, and how the different observed targets are distributed in depth.
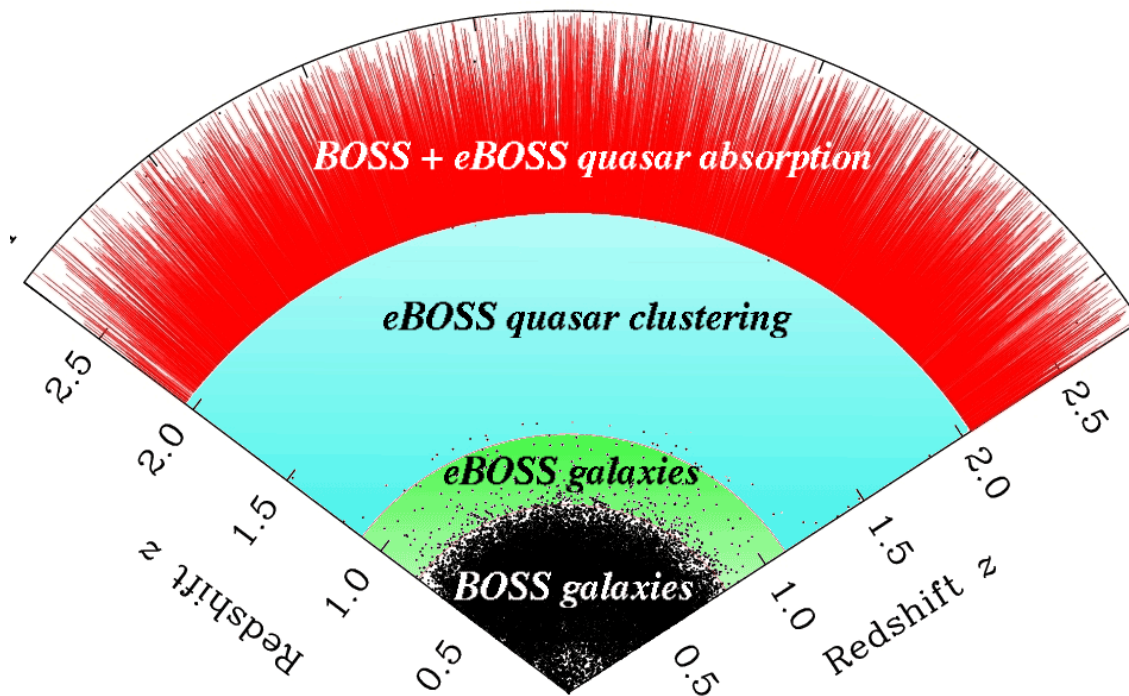
Figure 2.10

The fourteenth data release (DR14) is the second DR of SDSS-IV stage, and the fourteenth of SDSS, including data since it started operating in 2000 until 2018. This is also the first DR with eBOSS data. [2]

2.5.2 DESI

The *Dark Energy Spectroscopic Instrument* (DESI) is a wide area ground based experiment designed to study the BAO and growth of structure through redshift space distortions (RSD), and by the analysis of spectra of galaxies and quasars. It is the succesor of eBOSS and will overlap with

other surveys, such as the *Dark Energy Survey* (DES) and the *Large Synoptic Survey Telescope* (LSST). DESI is an instrument that is currently being installed at the prime focus of the 4 meter Mayall telescope in Kitt Peak, Arizona. It is a fiber fed spectrograph designed to take up to 5,000 spectra simultaneously, operated robotically. It is expected to observe in a range of wavelengths from 360nm to 980nm by fibers that feed ten three-arm spectrographs for a period of five years in which it will cover 14,000 deg^2. This survey will obtain more than 30 million galaxy and quasar spectra to measure the BAO and determine the matter power spectrum. The four kinds of dark matter tracers that will be observed are shown and explained in table 2.5.2. Figure 2.11 shows how deep in redshift is the DESI survey expected to be.

| Tracer	z range	Description
Luminous Red Galaxies (LRG)	$0.46 < z < 1$	Extension of the BOSS LRG survey in z.
Emission Line Galaxies (ELG)	up to $0.6 < z < 1.7$	Probation of the Uiverse at a higher redshift by targeting the galaxies that emit [OII].
Quasars	$2.1 < z < 3.5$	Tracers of the neutral hydrogen clouds and hence tracers of dark matter distribution via the Lyman-α forest (explained in the next section) in their spectra.
Bright Galaxy Survey (BGS)	$z \approx 0.2$	Magnitude limited survey of $\sim$ 10 million bright galaxies that will be done by DESI when the moonlight does not allow a good detection of the other mentioned tracers
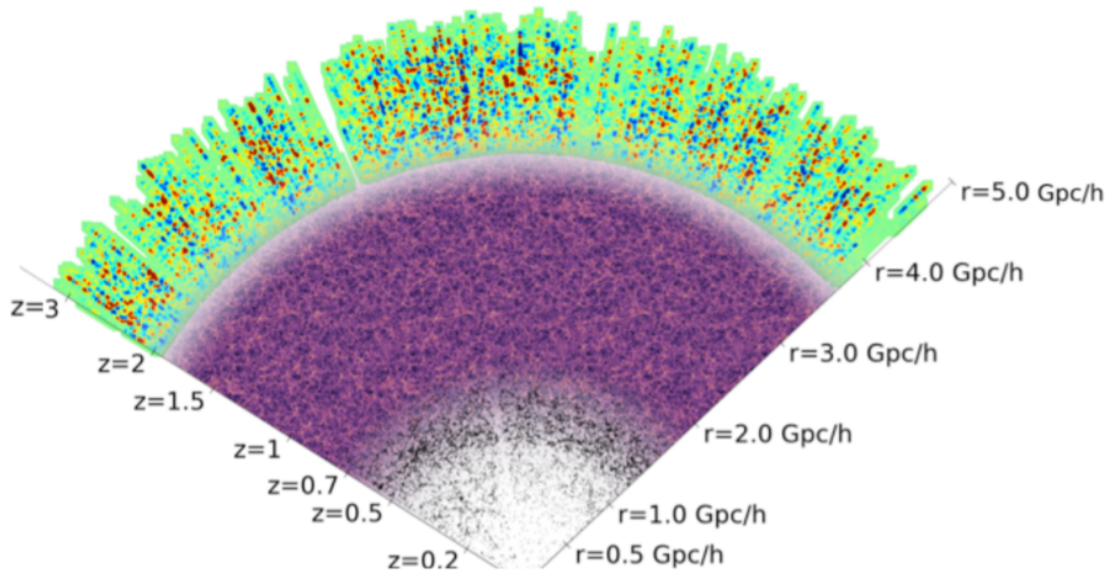
Figure 2.11: Depth of DESI survey in redshift and distribution of targets in redshift. From the center to the border, the white region represents 4 million LRGs, the purple one 18 million ELGs, the green 0.7 million Ly-α QSOs and the zone between the purple and green regions 1.7 million QSOs. [30]

Chapter 3

Lyman-α Forest Cosmology

3.1 Quasars

3.1.1 Active Galactic Nuclei

The term "normal" galaxies (as explained in the discusison made on [22]) refers to the ones with a spectrum predominated by the influence of stars. Their spectrum can be understood by the contribution of the black body radiation of all the individual stars in them. The spectrum of a "normal" galaxy is typically in the wavelength range of $\sim 4000\mathring{A}$ and $\sim 20000\mathring{A}$, which can be extended if it has active star formation (in smaller wavelengths) and heated dust (by these mentioned young stars).

There is a fraction of galaxies with a *spectral energy distribution* (SED) that is much wider than the wavelength range of a "normal" galaxy (even considering gas and stellar formation). Their range is from X-ray to radio and they often have strong and broad emission lines. These galaxies are known as *active galaxies*, and their activity comes from the central region, known as the *Active Galactic Nucleus* (AGN). The luminosity of the AGN, despite being a very small region, has luminosities that can be even a thousand times the host galaxy's.

According to Mo et al. ([22]), to define an object as an AGN one or more of the following properties should be observed:

- A compact nuclear region much brighter than a region of the same size in a normal galaxy

- Non-stellar (non-thermal) continuum emission

- Strong emission lines

- Variability in continuum emission and/or in emission lines on relatively short time scales

The active galaxies are classified into different types according to their observational properties: Seyfert galaxies, radio galaxies, quasars, BL Lac (BL Lacertae, named after its prototype) objects, and OVVs (optically violently variables). Examples of different AGN spectra are shown in figure 3.1.
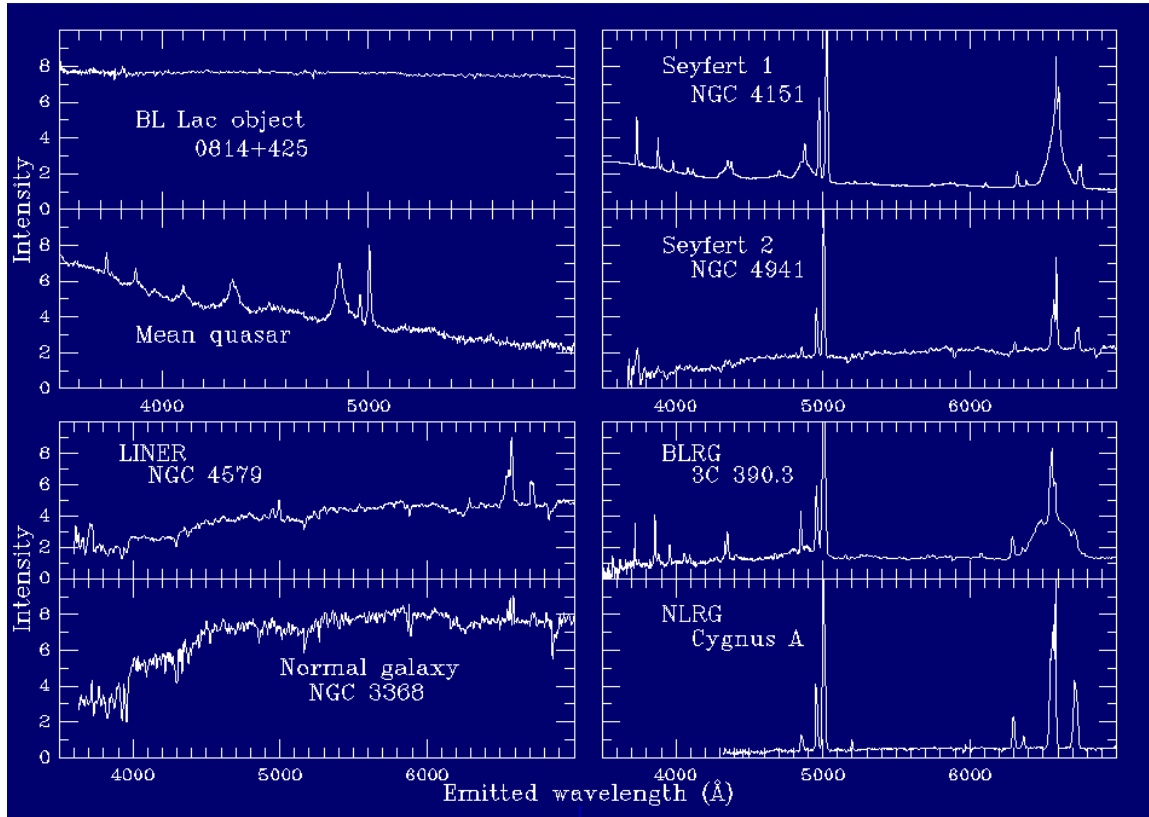
Figure 3.1: Examples of spectra of different types of Active Galactic Nuclei and a normal galaxy. Credit: Bill Keel. [31]

3.1.2   AGN spectra

The AGN spectra are made of two main ingredients: the continuum and the emission lines. The AGN spectra are boad, going from gamma rays up to radio. The overall SED can be described by a power law $F_\nu \propto \nu^{-\alpha}$, with $0 \leq \alpha \leq 1$. The SED also presents depressions and bumps, being the *blue bump* (at $\approx 10^{15}-10^{16} Hz$) and the *broad bump* (at $\approx 10^{20}-10^{21} Hz$) the most important/prominent ones. The wide energy range of the spectrum suggests there are many physical procesess behind their emission, most of them involving relativistic electrons.

   The relativistic electrons are thought to be generated in the first orfer Fermi accelerations that occur in shocks from supersonic flows near the central supermassive black hole (SMBH) in the center of the AGN. The Fermi acceleration is the acceleration that charged particles face when they are reflected (passing, scattering and repeated bouncing) by an interstelar magnetic field, resulting in a power-law energy distribution for the accelerated particles. The motion of these relativistic electrons with a power-law energy distribution in a magnetic field produces synchrotron radiation (generated by relativistic electrons spiraling in a magnetic field) with a power-law spectrum that can be of many decades in frequency in he radio band. The X-ray band energies are explained for photons emitted in inverse Compton process (that occurrs when a charged particle gives part of its

energy to a photon).

Emission lines are produced by the transitions of excited atoms. These lines are used to infer the physical properties of the emiting gas (density, temperature, composition, etc.) and the sources. Lines are divided into permitted and forbidden/improbable (there are some semiforbidden lines with intermediate spontaneous transitions) depending on the rate of spontaneous lines between energy levels responsible for the emission.

Line ratios are used to distinguish an AGN from a star-forming galaxy, which has emissions due to HII regions generated by young massive stars. The temperature and level of ionization are expected to be higher in an AGN because they have more UV flux, and because the radiation field in an AGN has more high energy photons.

3.1.3 Quasars and QSO

The term *quasar* comes from the term "Quasi-Stellar Radio Source", an it refers to compact radio sources with a non thermal continuum and strong, broad emission lines, and luminous nuclei that dominate in the blue/UV section of the spectrum and are often variable and sometimes have jets. thir luminosities can reach 1000 times the one of a normal galaxy. They usually outshine their host galaxy and it is very hard to observe, nonetheless nearby quasars have been detected in both, elliptical or spiral galaxies, and in dsiturbed interacting systems.

Usually the terms quasar and QSO are used indistintly, although the term *quasar* refers to a radio-loud source and *QSO* to a radio-quiet.

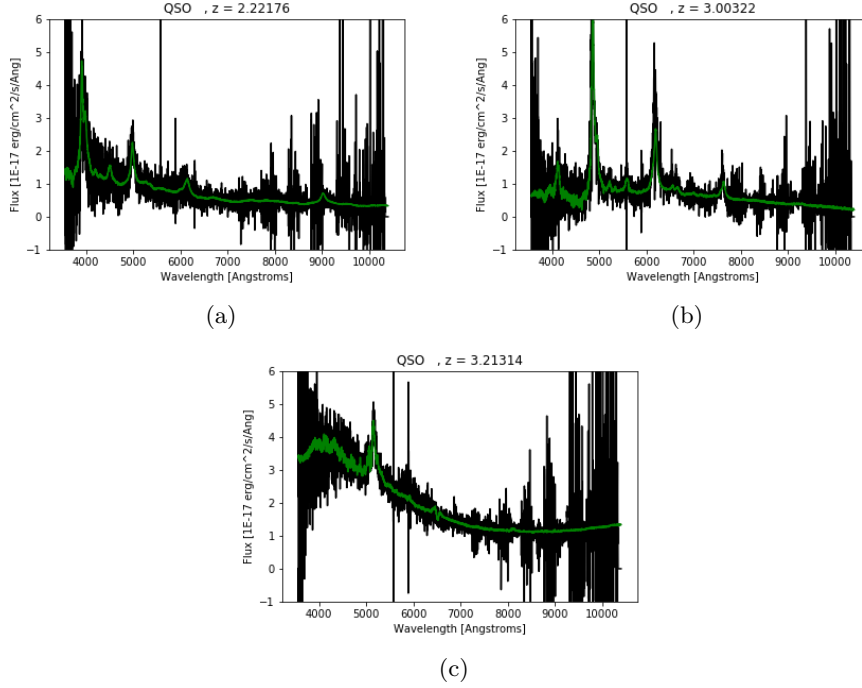Figure 3.2 shows examples of quasar spectra of eBOSS DR14.

(a)

(b)

(c)

Figure 3.2: Examples of spectra from eBOSS DR14. The black line represents the measured spectra, the green solid line represents the model. Plots obtained by Hiram Kalid Herrera Alcantar, División de Ciencias e Ingenierías, Universidad de Guanajuato.

3.2   Lyman-α Transition

The *Lyman series* is a spectral series of transitions in the hydrogen atom, occurring when an electron changes its energy level from $n \geq 2$ to $n = 1$. This transition causes the emission of photons in the ultraviolet range of the electromagnetic spectrum. Depending on the difference of the initial and final energy levels, a Greek letter is assigned to the corresponding transition; from $n = 2$ to $n = 1$ is called *Lyman-α*, from $n = 3$ to $n = 1$ is called *Lyman-β*, from $n = 4$ to $n = 1$ is called *Lyman-γ*, and so on.

   Among these, the Lyman-α transition occurs in the atoms conforming hydrogen clouds in the Inter Galactic Medium, where photons from a source (namely QSO) are absorbed, leaving their *fingerprint* in an absorption line at wavelength $\lambda = 1215.67 \mathring{A}$ in the spectra of the sources.

3.3   Lyman-α Forest

The *Inter Galactic Medium* (hereafter IGM) is made of clouds of gas, mainly hydrogen. In a much lower proportion there is also helium and traces of other elements, which are referred to as *metals*. The IGM is distributed in the Universe, situated in gravitational potential wells attributed to Dark Matter overdensities generated as a consequence of the evolution of primordial perturbations and

following the BAO theory explained before. The detection of these clouds is hence a tracer of dark matter distribution and behavior in the Universe.

Quasars are AGN with luminosities above $4\times10^{45}ergs^{-1}$ ($10^{12}L_{\odot}$), and are the brightest objects visible in galaxy surveys. As a consequence of their luminosities, they can be seen at high redshifts and their characteristic spectral lines are detected with high signal to noise ratio (S/N). As said before, IGM clouds are distributed through the Universe, if one of these clouds is found in the Line of Sight (LOS) between the quasar and the observer, it will leave the mentioned *fingerprint* in the spectrum of the quasar. Since the quasar is at high redshift z_q, the IGM will be distributed in clouds in a range of redshifts $0 < z < z_q$, hence the Lyman-α (Ly-α) absorption line corresponding to each IGM cloud will appear at their respective redshift. This allows to make an inference of the IGM distribution in that LOS (or skewer), as well as its density at different positions. If done over a big amount of spectra of quasars, this study allows to make a mapping of the IGM and by consequence of DM in the Universe, up to the reached z_q.

The figures below show schematically the absorptions of the QSO light by the IGM, originating the Ly-α forest. Figure 3.3 is a cartoon of the light being absorbed by clouds at different redshifts, and figure 3.4 shows how the presence of these clouds "builds" the Ly-α forest.

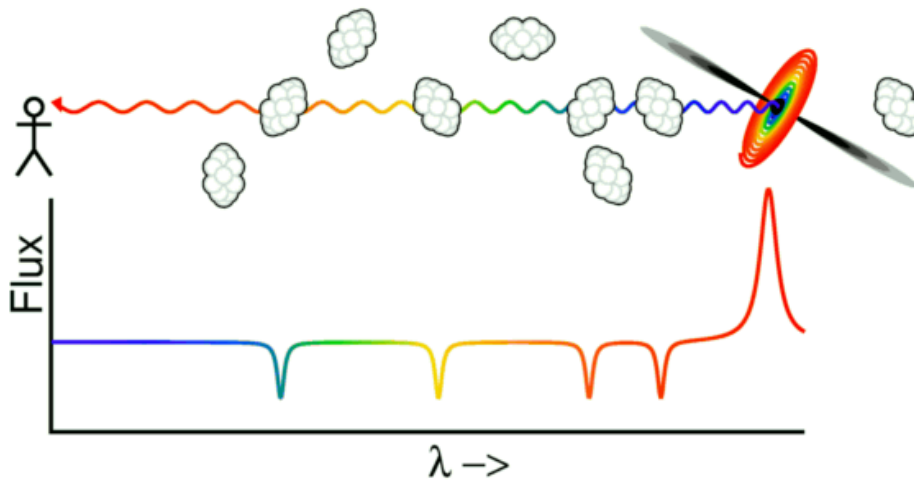Figure 3.3: Light emitted from a quasar at a high redshift is absorbed by IGM clouds at different redshifts on its way to the observer. These absorptions leave an imprint in the quasar measured spectrum. [32]
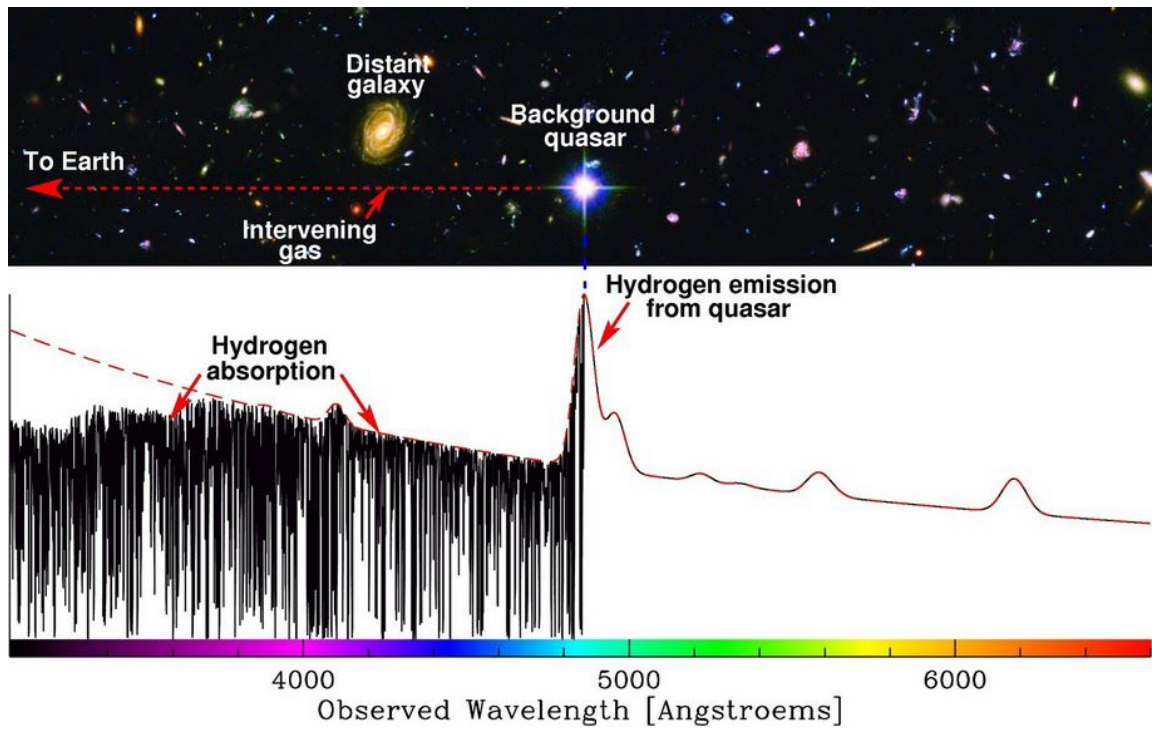
Figure 3.4: The light of a quasar at high redshift is absorbed by IGM clouds between it and the observer. Each of these clouds leaves an imprint in the spectra forming the Ly-α forest. [33]
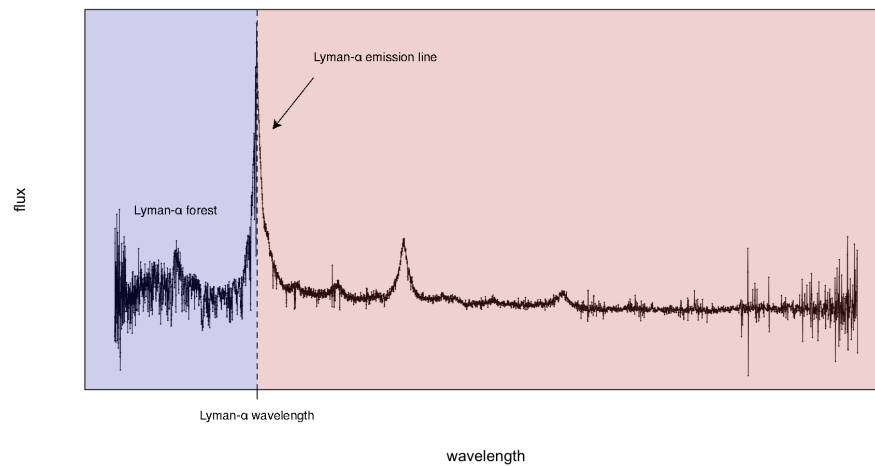

Figure 3.5

3.4 Lyman-α Forest in Cosmology

The BAO peak has been studied for several years, with different tracers at different redshifts, especially galaxies at $0.35 < z < 0.65$ with BOSS and other surveys, and eBOSS up to $z \approx 3$. At high redshifts, the BAO correlations are studied by the observation of quasars and their Ly-α forests (explained above) as mass tracers, allowing to study the correlations in the universe at $z \approx 2.4$.

3.4.1 Metals in the Lyman-α Forest

In the context of astronomy, the term *metallicity* refers to elements heavier than hydrogen and hellium. In this work, everything but the Ly-α transition is treated and referred to as a metal (even Ly-β), since they are absorptions contaminating the Ly-α forest. Metals in the IGM are observed in the QSO spectra as absorption lines. These absorptions are correlated with each other and with the Ly-α forest on characteristic scales, set by their wavelength ratios. This correlated signal potentially affects the LSS measurements in the forest contaminating the flux power spectrum $P(k)$ and flux correlation function ξ. (Slosar et al. 2011, [34])

To fully understand the $P(k)$ and ξ using the Lyman-α forest as tracer, synthetic data samples are generated (see section 3.8). In these synthetic samples (hereafter *Mock Catalogues*) there are diverse phenomena that can be simulated (such as high column densities, metallicity of the IGM, DLA, BALs, etc) as well as their effect in the flux $P(k)$ and ξ.

Bautista et al. (2017) [27] and du Mas des Borboux (2017) [?] report the effect of some of these phenomena in the flux $P(k)$ and ξ, simulated in a set of mocks and compared with eBOSS DR12. Metallic absoprtions are of peculiar interest, since the correlations among each other are observed as bumps in the ξ in wedges (explained below, see figure 3.6) $0.85 < \mu < 0.95$ and $0.95 < \mu < 1$ (especially the latter, because metallic correlations are observed with close spectra, which is visible in nearby lines of sight).

In this work, this effect reported by Bautista et al. (2017) is reproduced with the London Mocks (synthetic catalogue explained in section 3.8) and compared to eBOSS DR14.

3.5 Perturbations in the transmitted flux

The Ly-α forest was originally interpreted as the consequence of discrete gas clouds, but these are now understood as the absorptions of the continuous structure that conforms the filamentary structure. Hydrodynamic simulations are consistent with the hypothesis of a photoionized IGM with density fluctuations related to the primordial perturbations related to the distribution of galaxies and the CMB.

The Ly-α forest spectra are hence considered as a continuous field of Ly-α transmitted flux fraction $F(x)$ (x being the redshift space coordinate) related to the variations of density in the gas, peculiar velocities and temperature along the line of sight, and the primordial density field.

Given an adequate sample (dense and in a large volume, with a big amount of absorptions), the flux power spectrum can be computed. This power spectrum is related to the linear power spectrum of density perturbations as

$$P_F(k, \mu_k) = b_\delta^2 (1 + \beta \mu_k^2) P_L(k) \tag{3.1}$$

where P_L is the linear power spectrum of the mass density perturbations, μ_k is the cosine of the angle between the LOS and the wavevector $\vec{k}$ in Fourier space, b_δ is the bias factor that relates the

amplitude of observed (or simulated) fluctuations with those of the P_L, and β is related with how the mean value of F responds to peculiar velocities in the LSS (hence related with Redshift Space Distorsions - RSD).

The goal is to determine the shape of $P_L(k)$ for different scales and z and obtain measurements of cosmological parameters. b_δ and β can be determined at different redshifts and compared with the predictions of hydrodynamic simulations.

We define the variable

$$\delta_F(x) = \frac{F(x)}{\bar{F}} - 1 \tag{3.2}$$

where $\bar{F}$ is the mean value of F at a given redshift. Hereafter, all the statistics and correlation functions are a function of this variable. [35]

3.6   Power Spectrum $P(k)$ and Correlation Function ξ

Following the discussion in [22], the correlation function $\xi(r)$ describes the excess probability of finding two objects separated by a given distance x when compared to a random spacial distribution of these objects. The two-point flux correlation function is defined as:

$$\xi(r) = <\delta_1 \delta_2> \tag{3.3}$$

where $r = |\vec{x}_1 - \vec{x}_2|$ the separation between objects in comoving units, $< \cdots >$ represent the average of the ensemble, and the $\delta(x)$ represent the density perturbation field given by:

$$\delta(x) = \frac{\rho(x) - <\rho>}{<\rho>}, \tag{3.4}$$

being $\rho(x)$ the density distribution of matter at x. δ represents a homogeneous and isotropic random field. It can be expressed as $\delta(\vec{x}, t)$ or using its Fourier transform as $\delta_{\vec{k}}(t)$ as following:

$$\delta_{\vec{k}}(t) = \frac{1}{V} \int \delta(\vec{x}, t) e^{-i\vec{k} \cdot \vec{x}} d^3 \vec{x}, \tag{3.5}$$

being V the volume where the perturbation is assumed to be periodic. Using this expression, the correlation function can be expressed in terms of Fourier transforms of the δs as:

$$\xi(x) = \frac{1}{V} \sum_k P(k) e^{i\vec{k} \cdot \vec{x}} = \frac{1}{(2\pi)^3} \int P(k) e^{i\vec{k} \cdot \vec{x}} d^3 \vec{k} \tag{3.6}$$

where $P(k) = V < |d_{\vec{k}}|^2 >$ is the power spectrum.

3.7   Flux Correlation Functions ξ_F

A *pixel* is defined by bins Δr (redshift space separation), $\Delta \mu$ (angle cosine), and Δz (mean redshift), the set of these bins is A. The correlation function is defined as the weighted average of the product of δ in all pixel pairs in A, and it is given by the expression:

$$\hat{\xi}_A = \frac{\displaystyle\sum_{i,j \in A} w_i w_j \delta_{Fi} \delta_{Fj}}{\displaystyle\sum_{i,j \in A} w_i w_j},\tag{3.7}$$

where w_i is the weight for each pixel, given by the inverse of the total variance (sum of the variance of intrinsic Ly-α forest fluctuations, $\sigma_F^2(z) = \langle \sigma_F^2 \rangle$, and the one caused by the instrumental noise, $\sigma_N^2(\lambda)/[\bar{F}(z)C(\lambda)]^2$, being $C(\lambda)$ the QSO continuum) in each pixel as well, and expressed by:

$$w_i = \sigma_{-i}^2 = \left[\sigma_F^2(z_i) + \frac{\sigma_N^2(\lambda_i)}{\{\bar{F}(z_i)C(\lambda_i)^2\}} \right]^{-1}\tag{3.8}$$

To do the analysis of the correlations among pairs of pixels, two approaches of the correlation function are done: the one-dimensional (ξ_{1D}) and the three dimensional correlation function (ξ_{3D}).

3.7.1   One Dimensional Correlation Function ξ_{1D}

In the one dimensional Correlation Function ξ_{1D} the expression 3.7 is computed among pixels along the LOS, then averaged with all the other LOS. It is analyzed as a function of wavelength ratios λ_1/λ_2, where λ_1 is the biggest (i.e., the wavelength ratio $\lambda_1/\lambda_2 > 1$. The correlation among pixels corresponding to the metallic absorptions in the QSO spectra will be visible in the $\xi_1 D$ as peaks in their corresponding wavelength ratio (λ compared to $\lambda_{Ly-\alpha}$), as shown in figure 5.3.

3.7.2   Three Dimensional Correlation Function ξ_{3D}

In the three-dimensional Correlation Function $\xi_3 D$, expression 3.7 is computed considering pairs of pixels in the whole field (3D map of clouds), not considering which LOS they belong to. One can analyze the $\xi_1 D$ for the full sample ($0 < \mu < 1$), or different "wedges" of it (usually $0 < \mu < 0.5$, $0.5 < \mu < 0.8$, $0.8 < \mu < 0.95$ and $0.95 < \mu < 1$, being the two latter the most important for metal analysis, since the correlation among metallic absorptions are visible as we approach the LOS, which is $\mu = 1$, and "dillute" as μ decreases). Figure 3.6 shows schematically how different wedges look in the BAO radius.
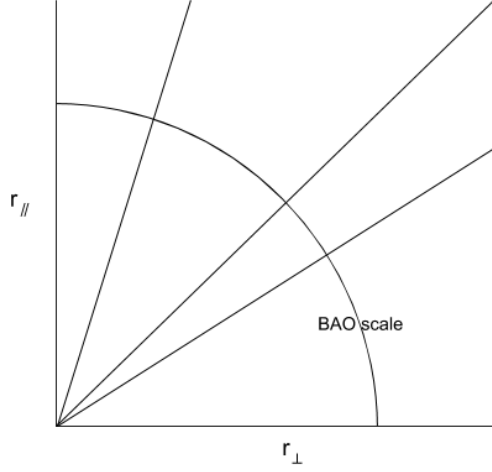
Figure 3.6: Four different wedges (defined by different values of μ in the interval between 0 and 1) are shown in an ideal BAO sphere projected in a plane.

3.7.3   Parameter Fits

There are different systematics and IGM contaminants that can affect the measured ξ for the mock catalogues when confronted with the one measured for the data. Among these, one of the clearest is the effect of the correlations of Ly-α absorptions with other transitions (Ly-β, Ly-γ, SiII, SiIII, OVI, CIV, and smaller contributions of other metals). When compared with a model, both the mock ξ and the data ξ independently present statistical biases b (one attributed to each transition). These two sets of biases b (the one measured for the data and the one measured for the mock catalogues) are compared, and this comparison helps to understand which systematics are important, and how much.

In order to quantify the effect of metals, the effect of each in the mock ξ is measured by their respective b. These values should be compared with what has been reported in other data releases and using different sets of mock catalogues, of particular interest are Bautista et al. (2017), du Mas des Borboux et al. (2017), and de Sainte Agathe et al. (2019).

3.8   Mock Data

The mocks that were used to compare with the data described above were generated and analyzed by a series of steps, each of them developed by a different code or package. The distribution of quasars was made by a lognormal matter density distribution simulation, next the flux transmission files of these, then turned into the spectra and conditions of DESI, and last the statistical study with IGM/Lya-forest analysis tools.

3.8.1 CoLoRe

The simulation to make the quasar mock catalogues was generated by a parallel C code called CoLoRe ([36], developed by David Alonso et al. (in prep.)), which is designed to make simplified simulations to test an analysis pipeline and studying the impact of systematics. This code uses a lognormal model for the matter density. It generates a gaussian density field at $z = 0$ using the linear power spectrum from CAMB ([37]), as well as its corresponding linear radial velocity field in a Cartesian grid. It then calculates the redshift of each point of this grid and linearly evolves both the density and velocity to that redshift, as well as redshift-dependent linear galaxy bias in the overdensity field evolution. The IGM clouds are then placed in the grid, which is then transformed to angular coordinates and redshift. Hence, with CoLoRe a whole sphere from $z = 0$ to $z = 3.7$ (equivalent to a box of $L \approx 10 Gpc/h$) is generated, with each cell of about $2 Mpc/h$. The output files of CoLoRe are skewers, with smooth spectra and no other structure on scales smaller than the cell size.

3.8.2 LyaCoLoRe

LyaCoLoRe [38] is a code developed by Farr et al. (in prep) in University College London to use CoLoRe outputs for generating simulated Lyman-α forest spectra. It takes the skewers made previously and transforms them into transmission files (where metals, associated with galaxies and high density regions are added) as following:

1. LyaCoLoRe takes the gaussian densities $\delta_G(x)$ generated by CoLoRe.

2. Since these skewers are smooth spectra, fluctuations corresponding to smaller structures also have to be simulated, hence an extra power is added, obtaining now $\delta_{Gextra}(x)$.

3. The densities $\rho(x)$ of the IGM are now simulated for each skewer.

4. Each of these densities is translated into an opacity τ associated with an hydrogen clouds where the Lyman-α transition occured, by the expresion:

$$\tau_{Ly-\alpha}(x) = A_{Ly-\alpha}\rho^{-\beta} \tag{3.9}$$

   where A is the absorption coefficient, and β is chosen so that the mean transmission and variance are similar to those of the data ([27]). In this stage, the skewer is computed in terms of opacities ($\tau_{Ly-\alpha}(x)$).

5. Until this step no radial velocities have been considered. All of the calculations have been made as a function of x. However, RSD should be considered to have more accurate simulations. The velocity of each skewer $v(x)$ is added, so that instead of having $\tau_{Ly-\alpha}(x)$, this quantity is transformed into $\tau_{Ly-\alpha}(s)$.

6. The opacity of the clouds can be transformed into flux F, following the expression:

$$F = e^{-\tau} \tag{3.10}$$

   Hence the skewers are now in terms of flux as $F_{Ly-\alpha}(\lambda)$, which are the transmission files, the final outputs of LyaCoLoRe.

These steps followed by LyaCoLoRe are schematically shown in *figure* 3.7

$$\delta_G(x) \longrightarrow \delta_{Gextra}(x) \longrightarrow \rho(x) \longrightarrow \tau_{Ly\text{-}\alpha}(x) \longrightarrow \tau_{Ly\text{-}\alpha}(s) \longrightarrow F_{Ly\text{-}\alpha}(\lambda) \longrightarrow$$

$$v(x)$$

$$F = e^{-\tau}$$

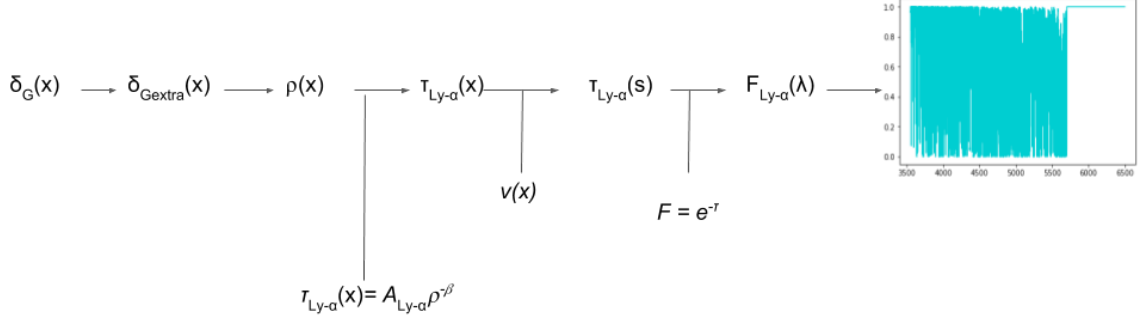$$\tau_{Ly\text{-}\alpha}(x) = A_{Ly\text{-}\alpha}\rho^{-\beta}$$

Figure 3.7: Scheme describing the process in which LyaCoLoRe generates flux transmission files from a lognormal matter density distribution simulation of quasars generated previously by CoLoRe.

Figure 4.4 shows an example of the transmission files for clouds where only the Lyman-α transition (i.e. just hydrogen) occurs.

3.8.3   Desisim/quickquasars

Desisim [39] (DESI collaboration (in prep.)) is a code developed to simulate spectra as if obtained with DESI. It takes the information from transmission files and, depending on the needs of the user, adds characteristics that allows certain features of the spectra to be analyzed - among these DLA, metals, fiber assignment and also atmospheric and light conditions due to the night sky in the observation date. These transmission files don't necessarily have to be generated by LyaCoLoRe (since the London Mocks are not the only, but the Saclay Mocks are also being developed), but the ones used for this work are. An important feature of Desisim in the specific case of adding metals to the spectra made from transmission files is that the absorptions of metals are added to the spectra after the effect of RSD is simulated, unlike LyaCoLoRe. This makes Desisim take shorter computing time and a more efficient tool for tests.

3.8.4   Data Analysis with PICCA and NERSC

PICCA (Package for IGM Cosmological-Correlations Analyses) [40] [41] [27] [42] [43] is a code that makes the Cosmological Analysis for Ly-α forest. It allows to understand the sample of quasars that is being used (spatial distribution in RA, DEC and z), view and compare the spectra of these quasars, calculate the Ly-α absorption (δ field), ξ_{1D}, auto (Ly-α-Ly-α, QSO-QSO) and cross (Ly-α-QSO) ξ_{3D}, ξ_{3D} wedges, and the best fit parameters (α, β, b, b_η) of the data used in the sample. This code was used to make all the cosmological analysis, results presented in the following chapters.

All the computation was made using the resources of the National Energy Research Scientific Computing Center (NERSC), which is the primary scientific computing facility for the Office of Science in the U.S. Department of Energy.

Chapter 4

Methodology

4.1 Data

Among the different Data Releases of the Sloan Digital Sky Survey, DR14 [2] are the most recent and best available data. The sample of data from this source used to compare with Mock catalogues are distributed in the footprint shown in figure 4.1 (considering that DR14 is cumulative and includes all three samples: BOSS, SEQUELS, and eBOSS), with a redshift distribution shown in figure 4.2.
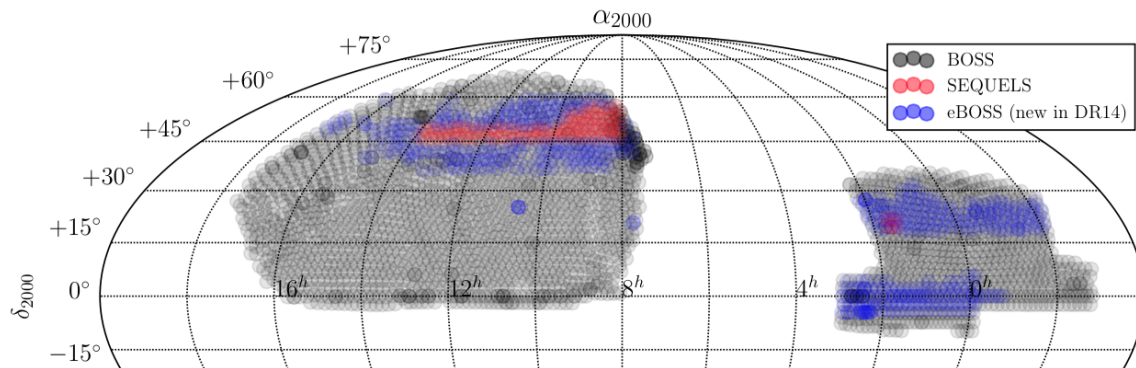

Figure 4.1: Footprint of the SDSS DR14 data. This cumulative DR includes the previous data of SDSS, and hence the three shown samples of the figure (BOSS, SEQUELS, and eBOSS). [2]
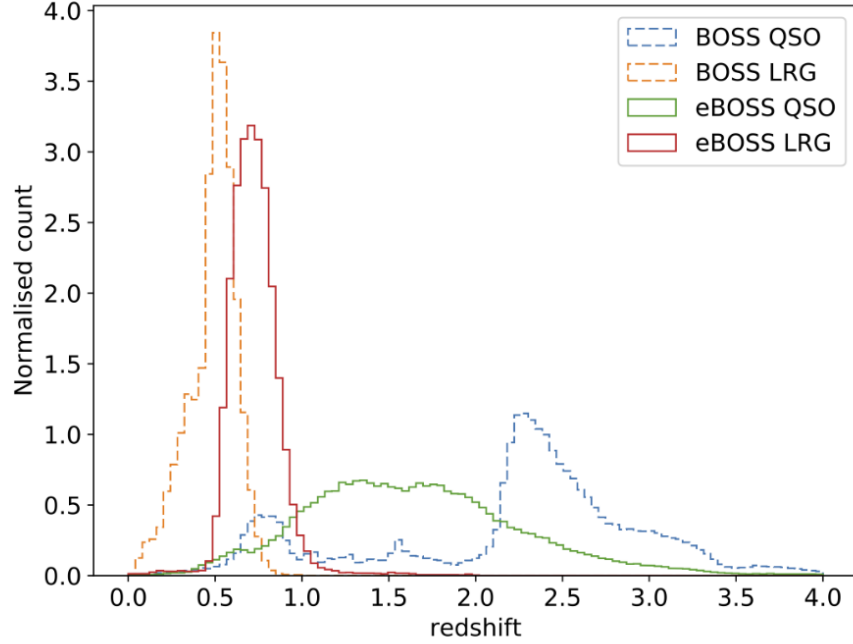
Figure 4.2: Histogram showing the distribution of LRGs and QSO samples measured by BOSS and eBOSS in DR14. [2]

4.2   Mocks

The mocks that were used to compare with the data described above were generated and analyzed by the tools exposed in the previous chapter: the distribution of quasars was made by a lognormal model for the density dsitribution simulation (CoLoRe), next the flux transmission files of these (LyaCoLoRe), then turned into the spectra and conditions of DESI (Desisim/quickquasars), and last the statistical study with IGM/Ly-α forest analysis tools (PICCA).

The research work that gave place to this document consists in (following the steps explained previously, developed by Alonso et al. ([36]) and Farr et al. (in prep., [38]), and the approach presented by Font-Ribera et al. (2011) [35] Bautista et al. (2017) [27] and Du Mas des Borboux et al. (2017) [42]) adding and studying the absorptions due to transitions other than Lyman-α added to LyaCoLoRe. These are referred to as "metals". The ones considered are Lyman-β and the elements shown in table 4.2 (see Table 2 in [27]), since these are the ones that strongly interact with the Lyman-α forest and bias the ξ_{1D}, ξ_{3D}, and ξ_{3D} wedges. The study of Si transitions is also important because their presence is an indicator of evolution of structure, namely stellar porcesess and the formation of galaxies.

Transition	Wavelength $\lambda[\mathring{A}]$
SiIII(1207)	1206.50
SiIIa(1190)	1190.42
SiIIb(1193)	1193.29
SiIIc(1260)	1260.42

The way the other lines were added was by following a parallel process as the one previously explained (see scheme in figure 4.3), but modifying the absorption coefficient A in step 4 so that instead of having 3.9, LyaCoLoRe also computed (for each skewer):

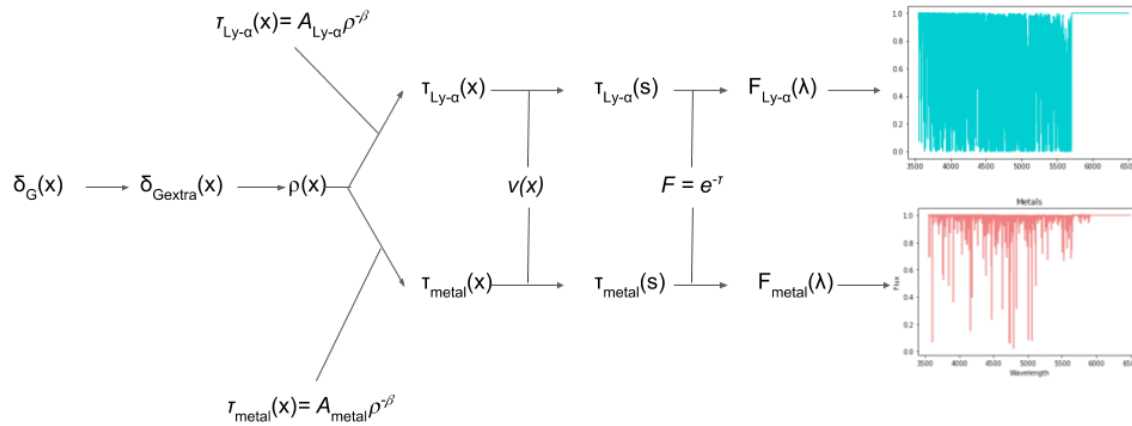$$\tau_{metal}(x) = A_{metal}\rho^{-\beta} \tag{4.1}$$

Figure 4.3: Scheme describing the process in which apsorptions due to metallic transitions are added LyaCoLoRe, and how the flux transmission files from the lognomal density distribution simulation of quasars generated previously by CoLoRe are generated.

Due to the computing time associated with each element added to LyaCoLoRe, the list of metals is reduced for the first tests (until the final version of London Mocks is developed and full computing resources are used) to the ones in Table 4.2, although the other metals to be included once these are succesfully added are the ones shown in the following table:

Transition	Wavelength $\lambda[\mathring{A}]$
NV(1243)	1242.804
NV(1239)	1238.821
NI(1200)	1200.000
OI(1039)	1039.230
OVI(1038)	1037.613
OVI(1032)	1031.912

Some examples of final transmission files for the computation of the flux are shown in the following figures: Figure 4.4 shows the flux with the absorption of only Ly-α transition, figure 4.5

shows the absorption due to Ly-β transitions, figure 4.6 shows the absorption due to both, Ly-α and Ly-β transitions , and figure 4.7 to the absorptions due only to Si transitions.
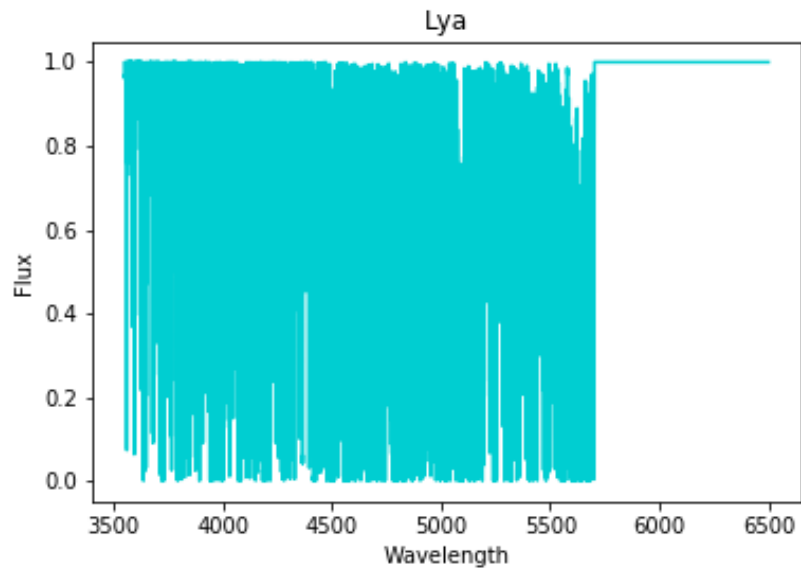

Figure 4.4: Transmission file made by LYACOLORE of a skewer where only the Lyman-α transition occurs.
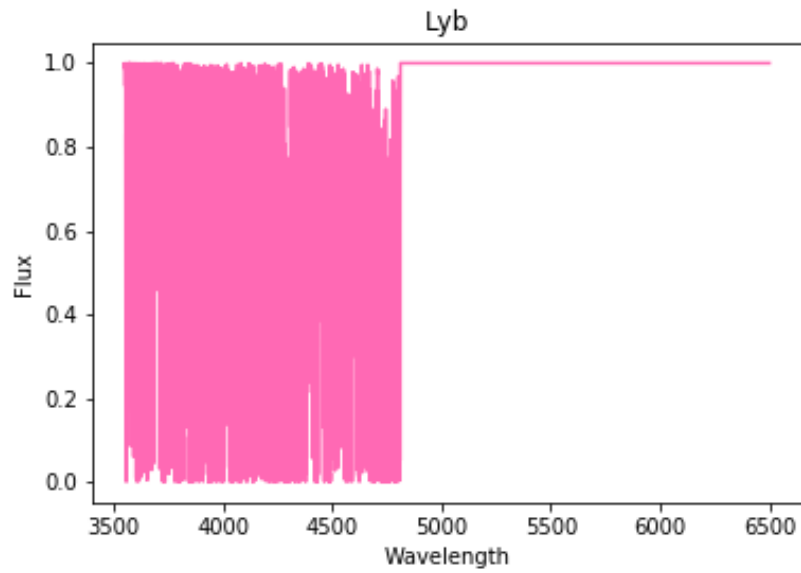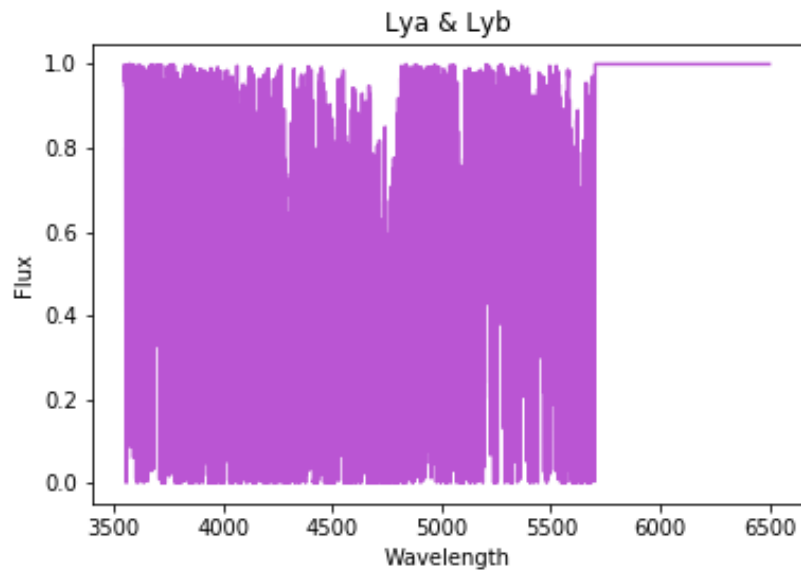
Figure 4.5: Transmission file made by LYACOLORE of a skewer where only the Lyman-β transition occurs.

Figure 4.6: Transmission file made by LYACOLORE of a skewer where Lyman-α and Lyman-β transitions occur.
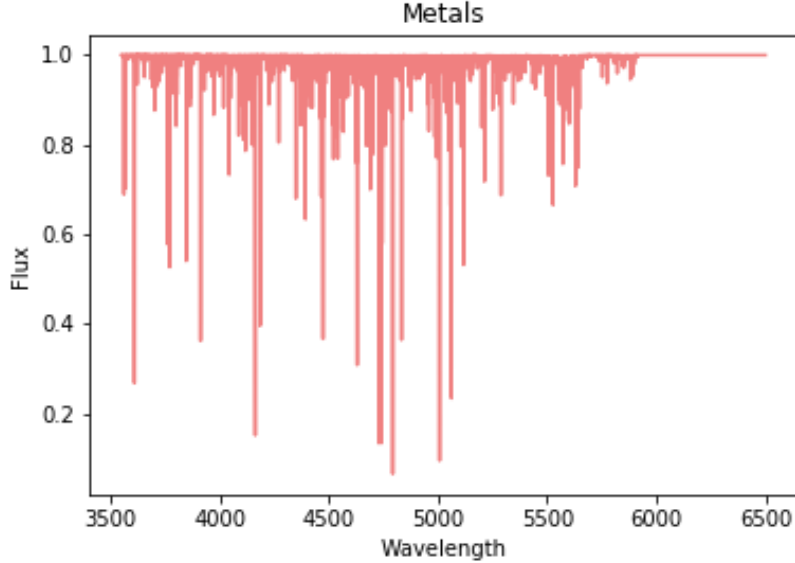
Figure 4.7: Transmission file made by LYACOLORE of a skewer where only metallic (in this case the four lines of Si in table 4.2) transitions occur.

In this work DESISIM (described in 3.8 in the previous chapter) was used in two stages: while DESISIM was being developed, the "*adding metals*" feature was implemented so they were added to the mock spectra after the effect of RSD was imprinted in them. When the metals were added in the transmission files, as mentioned earlier, this was done in a stage previous to the RSD effect. So the first stage of work wih DESISIM and LYACOLORE was comparing the spectra and the statistical analysis (ξ_{1D}, ξ_{3D} auto correlation functions) of the same sample of QSO, with metals added in both processes, and confronting both of them with data from eBOSS DR14. After analyzing these results (shown in the next chapter) it was clear that the absorption coefficients used previously were not precise values, and this quantity had to be tuned to fit the mocks to the data. This tuning was done for each Si transition (SiII(1260), SiIII(1207), SiII(1193), and SiII(1190)) adapting DESISIM code to increase this value as needed by multiplying it by a given factor (from 2 to 10), and then modifying these absorption coefficients while the mocks are being generated.

4.2.1   Mock data

With the tools explained in 3.8, several samples (numbered and explained below) of quasars were simulated.

To analyze the effect of metals in the IGM clouds, four catalogues of the London Mocks version 3 were made:

- v3.0/quick-0.0: Set of spectra with only Ly-α absorptions (no metals) from transmission files.

- v3.0/quick-0.2: Set of spectra with transmission files made as in quick-0.0, metals added via DESISIM.

- v3.2/quick-0.1: Set of spectra with Ly-α absorptions from transmission files, and one Si line SiII(1260)

- v3.3/quick-0.1: Set of spectra with Ly-α absorptions from transmission files, and four Si lines (SiII(1260), SiIII(1207), SiII(1193), and SiII(1190)).

The quasars making these samples are distributed in space in the footprint shown in figure 4.8. Their redshift distribution is shown in the histogram in figure 4.9.
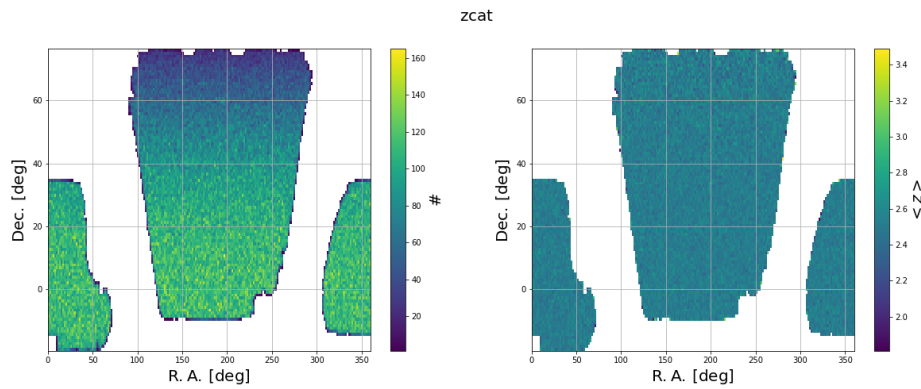

Figure 4.8: Distribution of QSO in RA and DEC of the London Mocks used for this study.
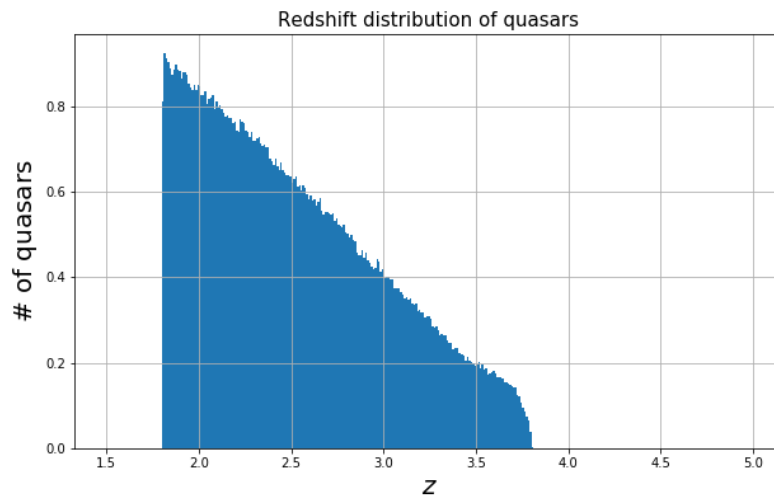

Figure 4.9: Histogram of the distribution of quasars in bins of redshift of the London Mocks used for this study.

Si Absorption coefficent tuning

To make the London Mocks more realistic comparing them with the data from DR14, it was necessary to tune the absorption coefficient values. To do this, a sample of the London Mocks version 3 with no metals was used, metals were added as needed by DESISIM as a first approach. The generated spectra are samples of $\approx$ 250,000 quasars with the following chracteristics:

- quick-0.0 All Si lines (SiII(1260), SiIII(1207), SiII(1193), and SiII(1190)) boosted by a factor of 10

- quick-0.1 SiII(1260) boosted by a factor of 5

- quick-0.2 SiIII(1207) boosted by a factor of 5

- quick-0.3 SiII(1193) boosted by a factor of 5

- quick-0.4 SiII(1190) boosted by a factor of 5

- quick-0.5 SiIII(1207) boosted by a factor of 2.5

- quick-0.6 First tuning of all Si lines from modification on DESISIM: SiII(1260) by a factor of 5, SiIII(1207) by a factor of 2.6, SiII(1193) by a factor of 5, and SiII(1190) by a factor of 5.

- quick-0.9 Tuning of all Si lines from modification on DESISIM comparing bias of quick-0.6 with citeVdSA: SiII(1260) by a factor of 5, SiIII(1207) by a factor of 4.8, SiII(1193) by a factor of 5, and SiII(1190) by a factor of 5.

These metals were first tuned in an artesanal way, trying the ξ_{1D} and ξ_{3D} $0.8 < \mu < 0.95$ and $0.95 < \mu < 1$ wedges (the ones closer to the LOS) to look as close as possible to the eBOSS data. There was a point where even the best tuning presented a bias twice as big than the one expected when compared to Bautisa et al. (2017), du Mas des Borboux et al. (2017) and de Sainte Agathe (in prep), or the bias got closer (1σ) but not the general behavior of the ξ. Considering the possible bias due to other phenomenae not yet added to the London Mocks in version 3, the tuning was made considering just the bias analysis and comparing the fitted ξ_{3D}. When eventually the further versions of London Mocks were avaliable, this approach made the tuning more efficient. The results to these adjustments are found in the next chapter.

Chapter 5

Results

5.1 Mocks vs data

The goal of adding metals to the Mock Catalogues is to make them more realistic, as well as understand them as contaminants of the Ly-α forest. Having that in mind, after the SiII(1260), SiIII(1207), SiII(1193), and SiII(1190) lines were added to the transmission files and made a spectra catalogue with the two ways of adding metals to the Mocks, they were then compared to data from eBOSS DR14. This was done with the following approach:

5.1.1 Mocks w/metals (1Si & 4Si vs data)

Four mock catalogues (explained in the Methodology) were compared:

- v3.0/quick-0.0: Set of spectra with only Ly-α absorptions (no metals) from transmission files.

- v3.0/quick-0.2: Set of spectra with transmission files made as in quick-0.0, metals added via DESISIM.

- v3.2/quick-0.1: Set of spectra with Ly-α absorptions from transmission files, and one Si line SiII(1260)

- v3.3/quick-0.1: Set of spectra with Ly-α absorptions from transmission files, and four Si lines (SiII(1260), SiIII(1207), SiII(1193), and SiII(1190)).

The analysis with PICCA was done for the four catalogues and the following plots were obtained:
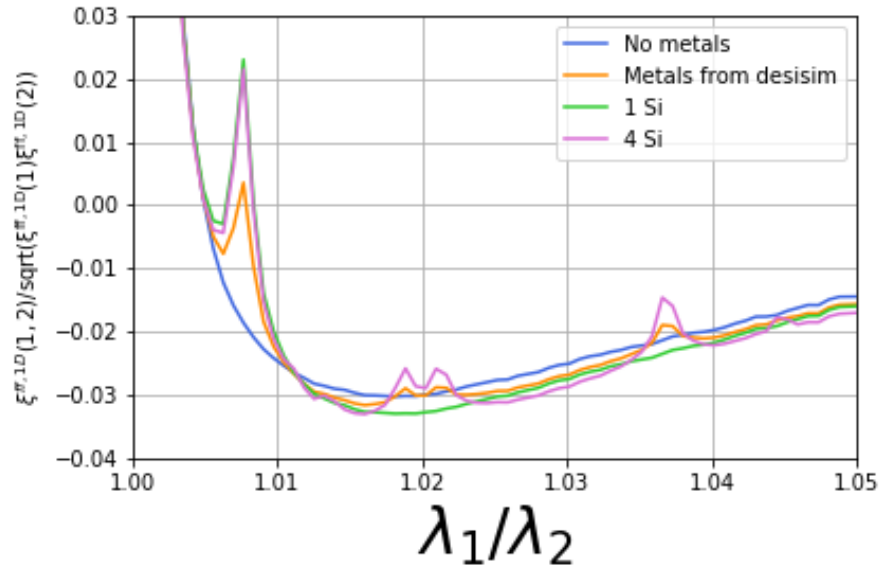
Figure 5.1: ξ_{1D} as a function of λ_1/λ_2, being λ_1 the one with the highest value of both. Four samples of London Mocks are compared: the blue line corresponds to a sample that has no metals, the orange one corresponds to the sample that has all the Si lines added via DESISIM, the green line corresponds to the sample that has the SiII(1207) added from transmission file, and the pink line to the one with all four Si lines added from the transmission file.

The first important visible result is that, as expected, when the metals are added from transmission files and to the spectra after RSD are modelled (via DESISIM) we obtain different correlations. It can be seen that the metals were added from the transmission file, the pixels with metallic absorptions were more correlated than when adding them via DESISIM.

The second important result is that when comparing the correlation function results with eBOSS DR14 (figure 5.2), it is clear that the absorption coefficients A are underestimated for some metals and overestimated for others, and these values should be adjusted.
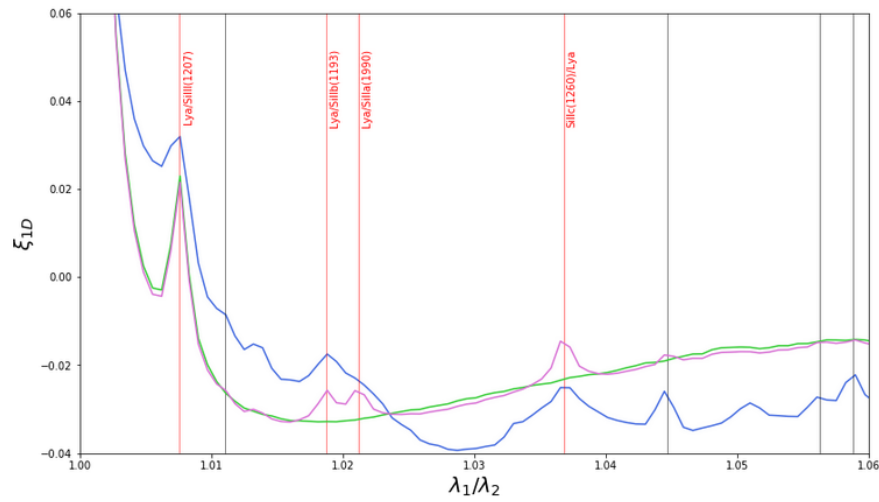
Figure 5.2: ξ_{1D} as a function of λ_1/λ_2, being λ_1 the one with the highest value of both. Two samples of London Mocks are compared: the green line corresponds to the sample that has the SiII(1207) added from transmission file, and the pink line to the one with all four Si lines added from the transmission file. The blue line corresponds to DR14 data. The red vertical lines point out where the λ_1/λ_2 of Si lines and Ly-α are located.
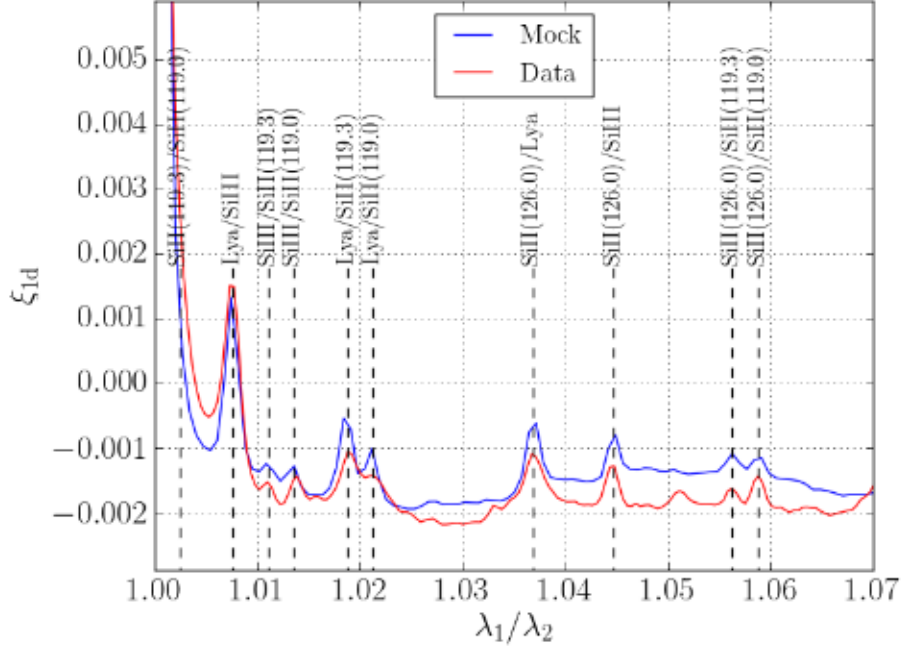
Figure 5.3: ξ_{1D} reported by Bautista et al. (2017) comparing DR12 with Mock data, pointing the λ_1/λ_2 for Si and Ly-α transitions. [27]

5.1.2   Adjustment of each Si line

Due to the lack of bibliography concerning IGM absorption coefficients A, and due to how different these values are expected to be according to the changes done in the Ly-α absorptions of each version of Mocks (particularly London Mocks), these values should be tuned in an artesanal way. This was done by making a modification in the DESISIM code, multiplying the A of all Si lines by a factor of 10 and each of the mentioned Si lines, one by one, by a factor of 5, and then individually, in different versions of the London Mocks, by an adaptation done to DESISIM explained below. The computed correlation functions for the range $0.95 < \mu < 1$ these adjustments is shown in figures 5.4 and 5.5.

Figure 5.4: ξ_{3D}'s $0.95 < \mu < 1$ wedge showing all the tunings of the absorption coefficients made for London Mocks v3. The red line represents is DR14 data, the black one the mock data with no metals, and all the other lines the different tunings.
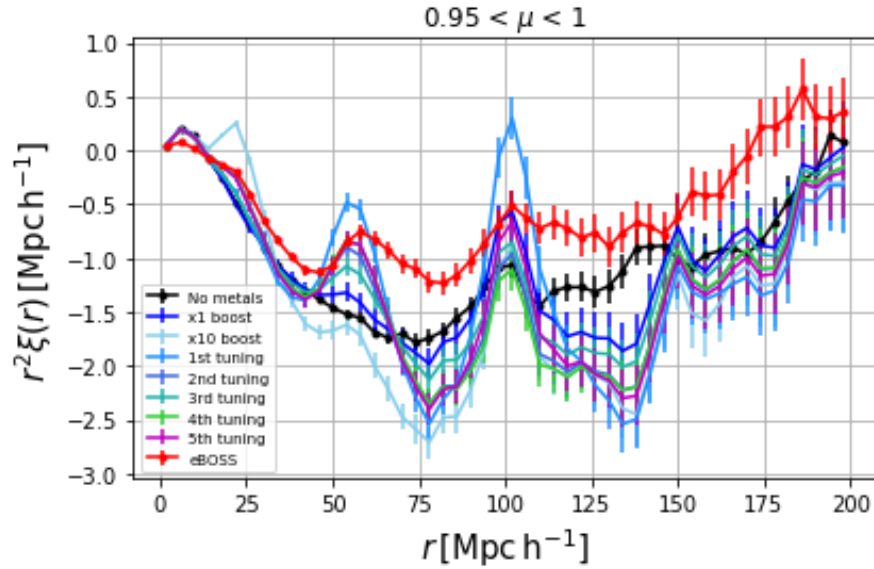

Figure 5.5: ξ_{3D}'s $0.95 < \mu < 1$ wedge showing all the tunings of the absorption coefficients made for London Mocks v3. The red line represents is DR14 data, the black one the mock data with no me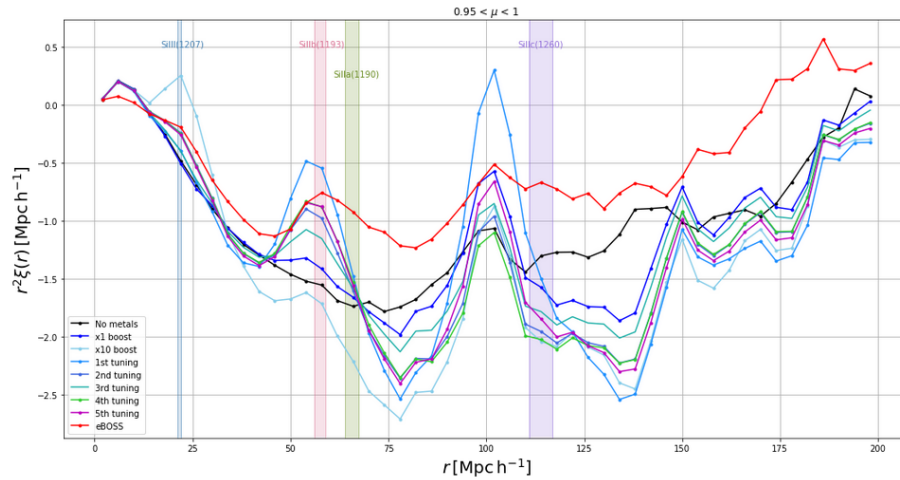tals, and all the other lines the different tunings. The vertical colored bars show the intervals of r where each metal affects the shape of the ξ_{3D}.

5.1.3   Desisim correction

According to the results of the ξ_{1D} shown in figures 5.1 and 5.2 the absorption coefficients A of each Si line were changed in the DESISIM code [39] as seen in figure 5.6.

```
6 ■■■■□ py/desisim/lya_spectra.py                                              View file   ∨

  ⚡        @@ -37,10 +37,10 @@
  37    37          'SiII(1260)'  : { 'LRF':1260.4221, 'COEF':3.542e-5 },
  38    38          'NV(1243)'    : { 'LRF':1242.804, 'COEF':5.e-4 },
  39    39          'NV(1239)'    : { 'LRF':1238.821, 'COEF':5.e-4 },
  40        -        'SiIII(1207)' : { 'LRF':1206.500, 'COEF':1.204e-3 },
        40  +        'SiIII(1207)' : { 'LRF':1206.500, 'COEF':1.8919e-3 },
  41    41          'NI(1200)'    : { 'LRF':1200., 'COEF':1.e-3 },
  42        -        'SiII(1193)'  : { 'LRF':1193.2897, 'COEF':5.193e-4 },
  43        -        'SiII(1190)'  : { 'LRF':1190.4158, 'COEF':5.999e-4 },
        42  +        'SiII(1193)'  : { 'LRF':1193.2897, 'COEF':9.0776e-4 },
        43  +        'SiII(1190)'  : { 'LRF':1190.4158, 'COEF':6.4239e-4 },
  44    44          'OI(1039)'    : { 'LRF':1039.230, 'COEF':1.e-3 },
  45    45          'OVI(1038)'   : { 'LRF':1037.613, 'COEF':3.382-3 },
  46    46          'OVI(1032)'   : { 'LRF':1031.912, 'COEF':5.358e-3 },
  ⚡
```

Figure 5.6: Modification of the DESISIM code with absorption coefficients tuned.

The fitted correlation functions of this adjustment, as well as its corresponding wedges (for the 6th version of London Mocks) are shown in figure 5.7 and 5.8.
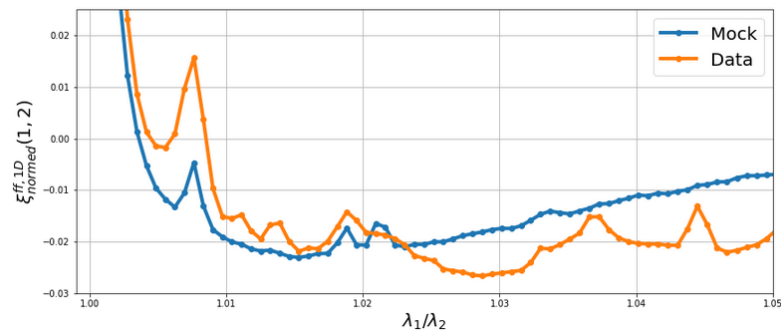

Figure 5.7: Fitted ξ_{1D} for DR14 data (in blue, computed by du Mas des Bourboux) and London Mocks v6's data (in orange) with all Si lines tuned.
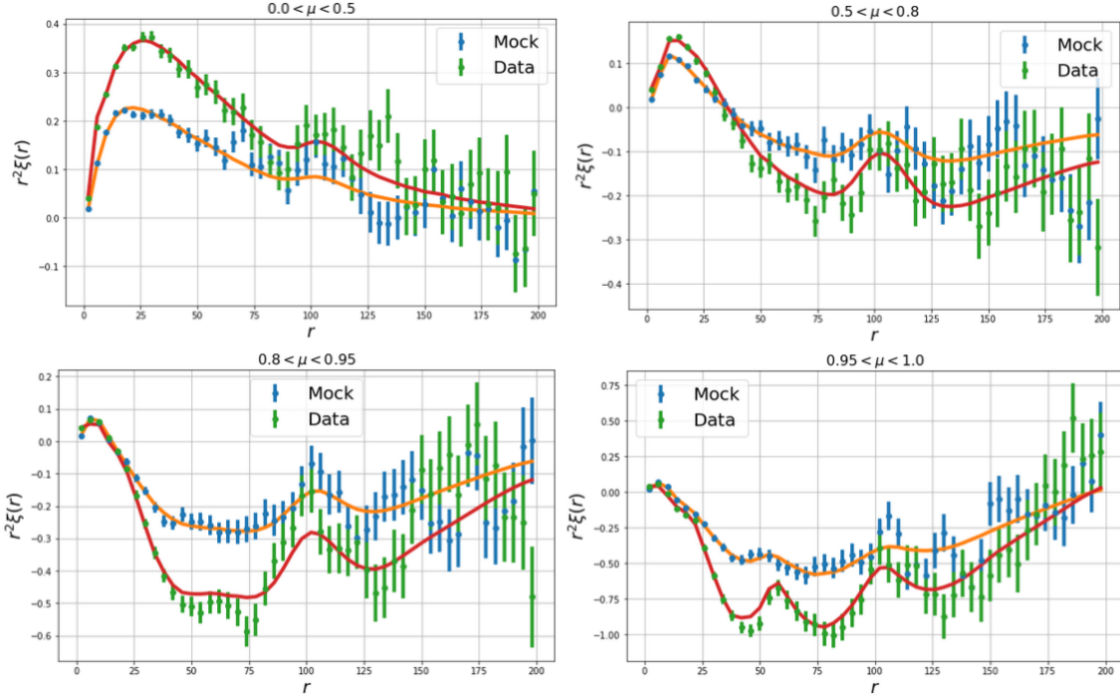
Figure 5.8: Fitted ξ_{3D} wedges for DR14 data (data in green, best fit in red, computed by du Mas des Bourboux) and London Mocks v6's data (data in blue, best fit in orange) with all Si lines tuned.

5.2 Comparing with previous work

The bias of each metallic absorption tuning was compared to results reported by Bautista et al. 2017, du Mas des Borboux et al. 2017 and de Sainte Agathe et al. (in prep). When compring all the computed biases with the mentioned work, a law that would allow to compute the correct value of A could be made, and now even though the London Mocks evolve, the metals' absorption would be tunned correctly according to the mentioned bibliography.

The values of Bautista et al. 2017, du Mas des Borboux et al. 2017 and de Sainte Agathe et al. (in prep) for the bias of each metal are shown in the following table:

Transition	Bautista et al. 2017	du Mas des Borboux et al. 2017	de Sainte Agathe et al. (in prep)
SiIII(1207)	-0.0033 ± 0.0013	-2.9 ± 1.1	-0.0080 ± 0.0010
SiIIa(1190)	-0.0044 ± 0.0009	-3.99 ± 0.83	-0.0050 ± 0.0010
SiIIb(1193)	-0.0035 ± 0.0009	-3.23 ± 0.84	-0.0046 ± 0.0010
SiIIc(1260)	-0.0015 ± 0.0012	-1.3 ± 1.1	-0.0022 ± 0.0013

This analysis, using eBOSS DR14 results (de Sainte Agathe et al. (in prep)) fixed the coefficients as shown in the next table:

Transition	Absorption coefficient A (coef)	Bias
SiIII(1207)	1.204×10^{-3}	-0.008 ± 0.001
SiIIa(1190)	5.999×10^{-4}	-0.005 ± 0.001
SiIIb(1193)	5.193×10^{-4}	-0.0046 ± 0.001
SiIIc(1260)	3.542×10^{-5}	-0.0022 ± 0.003

Chapter 6

Discussion

6.1 Adding Metals to Tansition Files

6.1.1 Comparison Between Metal Adding Methods

The most relevant tests to study if the simulated metalicity of the IGM are the right explanation for the features observed in the data are the ξ_{3D} wedges closest to the LOS, as well as the ξ_{1D}. Slice plots close to the LOS are also used to understand this, but are more often used to crumble the cross-correlation functions. Nonetheless, there are still improvements done in each version of the London Mocks. This is why the tunings are done trying to approach the biases due to each metal, so that when the other possible phenomenae that affect the statistics and the correlation functions are added to the mocks, the metals are correctly tunned (or closely, since they can be moved when including these other features).

The first test was analyzing the two techniques to add metals (via DESISIM and from transmission files) and confronting them with each oher in the ξ_{1D}. This (figure 5.1) showed that when the metals were added from the transmission file, the pixels with metallic absorptions were more correlated than when adding them via DESISIM. The best explanation for this is that DESISIM adds the absorptions after other phenomena that affect the spectra are simulated, and LYACOLORE adds the metals to the transmission files before adding the effect of RSD. As a consequence, this shifts the positions of the absorptions and biases the correlations of pixels, hence appear to be underestimated when comparing with lines added in LYACOLORE. When confronting the transmission file method with eBOSS data (figure **??**, it can be seen that SiIII(1207), SiII(1190), and SiII(1193) appear to be underestimated, while SiII(1260) appears to be the opposite case.

6.2 Metal Tuning Analysis

As explained in the results, the over and under estimation of the absorption coefficients of the four metal lines lead to the need to tune the values of the absorptions of each metal. Even though the first approach for this tuning was in the ξ_{1D}, it was thoroughly discussed that the best option was to do so in the ξ_{3D}, both by eye and using the values of the fitted biases for each Si transition. Figures 5.4 and 5.5 show these tunings in v3 of London Mocks. After reaching the best value for the biases and not managing to get any closer tto the biases reported by Bautista et al. 2017 while

still being an order of magnitude too high, after several tunings v5 and v6 of London Mocks were used. For these, the different values used for the absorption coefficients (A, also reported as $coef$) and the biases obtained after each run were plotted and compared with Bautista et al. 2017, du Mas des Borboux et al., and de Sainte Agathe et al. (in prep). With this a general behavior was fitted as a linear law which allowed to use the latter data, and find the value of A for the wanted bias. A sample of spectra of London Mocks v6 was taken to add these tunings, and the obtained best fit model for this sample are shown in figure 5.8

As said before, the tests to analyze the metal tunings are the wedges close o the LOS, and hence the plots for this discussion are these. Figures 5.7 and 5.8 show the fitted ξ_{3D} for wedges $0.8 < \mu < 0.95$ and $0.95 < \mu < 1$, as well as the ξ_{1D}. It is seen in the ξ_{3D} that the fitted models (the solid lines) are closer to the data than the analysis with the previous versions. There is, though, some flatness in the peaks of the ξ_{3D} attributed to SIII(1190), SiII(1193), and SiII(1260). Nonetheless, if one observes the data points and not the solid lines, one can see that the behavior is not so distant between eBOSS data and Mock data. Further analysis with bigger samples and improved versions of mock data are expected to fix this discrepancy.

Of course finer tunings can be made, and the fits might change when taking bigger samples. Nonetheless, the computing time in NERSC can increase from 40 min to compute the ξ_{3D} and around half a day queuing for the job to run, to over four hours of computing and probably more than two days in the waiting list. Currently, a final sample of half a million spectra is being analyzed by PICCA so that the best computed values are modified in LyaCoLoRe and include tuned metals in the next version of the London Mocks.

As part of this study, other metallic lines are currently being added, and other auto and cross correlations are also being computed and hopefully in a near future can also be added to the transmission files before the London Mocks v8 are produced.

Chapter 7

Further work

7.1 Adding other metals

As a first approach, Si explains some of the "bumps" and "anchores" in the ξ_{1D} and ξ_{3D} since it is the most visible contmainant in the Ly-α forest. Nonetheless, when analyzing other correlations, forests and absorbers (for example the effect of the CIV doublet in the Ly-α forest, or the OVI doublet in the Ly-β forest) one can see that a similar task should be implemented to tune these absorptions. This work is currently being done (under the collaboration and supervision of Helion du Mas des Borboux) so that these metals can be added in the London Mocks.

7.2 Pipeline

Running DESISIM and PICCA (steps to follow between making a change in a metal's coefficient and obtaining ξ_{1D}, ξ_{3D}, ξ_{3D} wedges, and fits of the data) require the execution of many commands in the NERSC console, among those some can take minutes or maybe even hours to queue and run, especially when the QSO samples involve several hundreds of thousands of objects (and even over a million). To optimize these times it was necessary to generate a pipeline, which condensates all these commands into four scripts, hence to the execution of two commands in the console. Not only this makes the execution more efficient, but also the tuning of each metal's absorption coefficient for each of the further mock versions.

7.3 Tuning of metalic absorption lines in LyaCoLoRe

The tuning of the absorption coefficients A in this analysis has been made in DESISIM because it requires less computational resources to do, but it has been explained and tested that the most accurate way of adding metals is from the transmission files, which is doing so in LYACOLORE instead of DESISIM (mainly because this would happen before RSD effect is added, and in DESISIM it happens the opposite way). The next step for the further versions of London Mocks concerning metals is adding the different values found for A in DESISIM with this work and the pipeline presented in the previous section, in LYACOLORE.

7.4   PICCA manual and documentation

PICCA is a package of computational tools developed by a group of people, which is currently in its third version (PICCA - Theoderic). Despite the multiple and very valuable efforts of developing such a package, and the constant support given online for users, there is no documentation on how to use it except for a tutorial to learn the basic steps to run PICCA over a sample of QSO, and the self-contained help for certain features and options of the different scripts. When speaking of making analysis on IGM lines other than Ly-α, there is no extra documentation at all. The work developed in this thesis hepled to find this problem, and solve it by starting to develop a manual to use PICCA.

Chapter 8

Conclusions

It has been noticed since the earliest of eBOSS DR that wedges of the flux ξ_{3D} closest to the line of sight presents *bumps* (excess of correlations) at different scales. Throug the years this has been explained by the pressence of absorption lines of metals in the Ly-α forest. These metals are treated as *contaminants*, and its understanding has become important to explain the general behavior of the ξ_{3D} and ξ_{1D}.

From this work it can be seen (as reported in articles of eBOSS DR12 and DR14) that the pressence of Si in the IGM modifies the shape of the ξ_{3D} and ξ_{1D}. This is observed as a *bump* in the scale of $60Mpc/h$, an increase in the correlations near the BAO peak, and an anchor at $20Mpc/h$ in the $0.8 < \mu < 0.95$ and $0.95 < \mu < 1$ wedges of the ξ_{3D}, and in the ξ_{1D} as peaks in the wavelength ratios corresponding to each of the Si lines used for this study.

The main peak in the ξ_{1D} (tending to ∞ as $\lambda_1/\lambda 2$ tends to 1) corresponds to the correlation of pixels of redshifted Lyα transition absorption lines in a LOS, averaged in all of them. When adding metals, the correlations between pixels with Si lines and Lyα, and Si lines with Si lines are computed as an "excess" of correlation at these wavelengths, and hence look as peaks in the ξ_{1D}.

The peaks in the $0.95 < \mu < 1$ wedge of the ξ_{3D} correspond to the "excess" of correlation due to each Si transition; the anchor near $20Mpc/h$ is due to SiIII(1207), the bump at $60Mpc/h$ is due to the correlations involving SiII(1190) and SiII(1193) (which are highly correlated with one another as well), and the "extra" correlation on top of the BAO peak at $100Mpc/h$ to SiII(1260).

Adding these lines to the Mock spectra makes them indeed more realistic (being this the main goal of understanding them as contaminants), and together with the development of the other features (DLA, BALS, HCD etc.) in the different versions of the Mocks, they allow a better analysis of the eBOSS DR14 data and further.

Bibliography

[1] K. S. e. a. Dawson, "The SDSS-IV extended Baryon Oscillation Spectroscopic Survey: Overview and Early Data," *Astron. J.*, vol. 151, p. 44, 2016.

[2] S. Collaboration, "The Fourteenth Data Release of the Sloan Digital Sky Survey: First Spectroscopic Data from the Extended Baryon Oscillation Spectroscopic Survey and from the Second Phase of the Apache Point Observatory Galactic Evolution Experiment," *The Astrophysical Journal Supplement Series*, vol. 235, p. 42, Apr 2018.

[3] A. e. a. Aghamousa, "The DESI Experiment Part I: Science,Targeting, and Survey Design," 2016.

[4] A. e. a. Aghamousa, "The DESI Experiment Part II: Instrument Design," 2016.

[5] D. E. S. Instrument, "Cosmology and dark energy." https://www.desi.lbl.gov/, https://www.desi.lbl.gov/cosmology-and-dark-energy/.

[6] N. Aeronautics and S. Administration, "Lambda-education." https://lambda.gsfc.nasa.gov/education/graphic$_h$istory/univ$_e$vol.cfm.

[7] M. White, "Big bang nucleocynthesis." http://w.astro.berkeley.edu/ mwhite/darkmatter/bbn.html.

[8] P. Collaboration, "Planck 2018 results. vi. cosmological parameters," *arXiv preprint arXiv:1807.06209*, 2018.

[9] G. F. e. a. Smoot, "Structure in the COBE differential microwave radiometer first year maps," *Astrophys. J.*, vol. 396, pp. L1–L5, 1992.

[10] C. B. Netterfield *et al.*, "A measurement by Boomerang of multiple peaks in the angular power spectrum of the cosmic microwave background," *Astrophys. J.*, vol. 571, pp. 604–614, 2002.

[11] B. Rabii *et al.*, "MAXIMA: A Balloon - borne Cosmic Microwave Background anisotropy experiment," *Rev. Sci. Instrum.*, vol. 77, p. 071101, 2006.

[12] M. C. Runyan *et al.*, "The Arcminute Cosmology Bolometer Array Receiver," *Astrophys. J. Suppl.*, vol. 149, p. 265, 2003.

[13] C. L. Bennett *et al.*, "The Microwave Anisotropy Probe (MAP) mission," *Astrophys. J.*, vol. 583, pp. 1–23, 2003.

[14] K. S. Dawson, D. J. Schlegel, C. P. Ahn, S. F. Anderson, É. Aubourg, S. Bailey, R. H. Bark-houser, J. E. Bautista, A. r. Beifiori, and A. A. Berlind, "The Baryon Oscillation Spectroscopic Survey of SDSS-III," , vol. 145, p. 10, Jan 2013.

[15] M. J. Drinkwater, R. J. Jurek, C. Blake, D. Woods, K. A. Pimbblet, K. Glazebrook, R. Sharp, M. B. Pracy, S. Brough, and M. Colless, "The WiggleZ Dark Energy Survey: survey design and first data release," , vol. 401, pp. 1429–1452, Jan 2010.

[16] K. Honscheid and D. L. DePoy, "The Dark Energy Camera (DECam)," 2008.

[17] I. Sevilla, R. Armstrong, E. Bertin, A. Carlson, G. Daues, S. Desai, M. Gower, R. Gruendl, W. Hanlon, and M. Jarvis, "The Dark Energy Survey Data Management System," *arXiv e-prints*, p. arXiv:1109.6741, Sep 2011.

[18] D. H. e. a. Jones, "The 6dF Galaxy Survey: Samples, observational techniques and the first data release," *Mon. Not. Roy. Astron. Soc.*, vol. 355, pp. 747–763, 2004.

[19] G. Goldhaber, "The Acceleration of the Expansion of the Universe: A Brief Early History of the Supernova Cosmology Project (SCP)," in *American Institute of Physics Conference Series* (D. B. Cline, ed.), vol. 1166 of *American Institute of Physics Conference Series*, pp. 53–72, Sep 2009.

[20] D. M. Scolnic *et al.*, "The Complete Light-curve Sample of Spectroscopically Confirmed SNe Ia from Pan-STARRS1 and Cosmological Constraints from the Combined Pantheon Sample," *Astrophys. J.*, vol. 859, no. 2, p. 101, 2018.

[21] E. W. Kolb and M. S. Turner, *The Early Universe*, vol. 69. 1990.

[22] H. Mo, F. C. van den Bosch, and S. White, *Galaxy Formation and Evolution*. May 2010.

[23] M. e. a. Boylan-Kolchin, "Resolving cosmic structure formation with the Millennium-II Simulation," , vol. 398, pp. 1150–1164, Sep 2009.

[24] V. Springel, C. S. Frenk, and S. D. M. White, "The large-scale structure of the Universe," *Nature*, vol. 440, p. 1137, 2006.

[25] T. D. E. Survey, "Large scale structure." https://www.darkenergysurvey.org/supporting-science/large-scale-structure/.

[26] C. for Astrophysics and Supercomputing, "Evolution of perturbations through different stages of the universe." http://astronomy.swin.edu.au/cms/imagedb/albums/scaled$_c$ache/$cmbFinal_sam_small$ − $280x396.jpg$.

[27] J. E. Bautista *et al.*, "Measurement of baryon acoustic oscillation correlations at $z = 2.3$ with SDSS DR12 Lyα-Forests," *Astron. Astrophys.*, vol. 603, p. A12, 2017.

[28] A. e. a. Heavens, "Standard rulers, candles, and clocks from the low-redshift Universe," *Phys. Rev. Lett.*, vol. 113, no. 24, p. 241302, 2014.

[29] S. Collaboration, "Sloan digital sky survey: Early data release," *The Astronomical Journal*, vol. 123, pp. 485–548, jan 2002.

[30] P. McDonald, "Desi: The dark energy spectroscopic instrument." https://commons.lbl.gov/display/physics/, http://www-physics.lbl.gov/seminars/old/McDonald.pdf.

[31] T. S. A. O. E. o. A. Cosmos, "Active galactic nuclei." http://astronomy.swin.edu.au/cosmos/A/Active+Galactic+Nuclei.

[32] E. L. Wright, "Prof. edward l. (ned) wright." http://www.astro.ucla.edu/ wright/intro.html, http://www.astro.ucla.edu/%7Ewright/lyaf-75.gif.

[33] "Lyman-alpha forest." http://www.futura-sciences.us/, http://www.futura-sciences.us/dico/d/physics-lyman-alpha-forest-50003899/.

[34] F. A. e. a. Slosar, Anže, "The Lyman-α forest in three dimensions: measurements of large scale flux correlations from BOSS 1st-year data," *Journal of Cosmology and Astro-Particle Physics*, vol. 2011, p. 001, Sep 2011.

[35] A. Font-Ribera, P. McDonald, and J. Miralda-Escudé, "Generating mock data sets for large-scale Lyman-α forest correlation measurements," *Journal of Cosmology and Astro-Particle Physics*, vol. 2012, p. 001, Jan 2012.

[36] D. Alonso, "https://github.com/damonge/colore." https://github.com/damonge/CoLoRe.

[37] A. Lewis, A. Challinor, and A. Lasenby, "Efficient computation of CMB anisotropies in closed FRW models," *Astrophys. J.*, vol. 538, pp. 473–476, 2000.

[38] J. F. et al., "Lyacolore." https://github.com/igmhub/LyaCoLoRe, in prep.

[39] D. collaboration, "desisim." https://github.com/desihub/desisim, in prep.

[40] "Package for igm cosmological-correlations analyses." https://github.com/igmhub/picca, in prep.

[41] M. e. a. Blomqvist, "The triply-ionized carbon forest from eBOSS: cosmological correlations with quasars in SDSS-IV DR14," *JCAP*, vol. 1805, no. 05, p. 029, 2018.

[42] H. e. a. du Mas des Bourboux, "Baryon acoustic oscillations from the complete SDSS-III Lyα-quasar cross-correlation function at $z = 2.4$," *Astron. Astrophys.*, vol. 608, p. A130, 2017.

[43] H. e. a. du Mas des Bourboux, "The extended Baryon Oscillation Spectroscopic Survey: measuring the cross-correlation between the MgII flux transmission field and quasars and galaxies at $z = 0.59$," 2019.